Check for updates

Synthesis of high-entropy alloys for electrocatalysis

Alexander Li, Nayla Qureshi and Vivek Maheshwari 🆔 *

High entropy alloys have garnered significant research interest in the field of electrochemistry in recent years due to their unique catalytic properties. These materials, characterized by a multi-principal element composition, have demonstrated superior catalytic performance and enhanced stability compared to traditional catalysts. However, the inherent complexity of high entropy alloys poses significant challenges, particularly in two key areas. First, this complexity makes studying and fully understanding the material's properties and behavior difficult. Second, the synthesis of nanoscale high entropy alloys is often complex, costly, and differs substantially from their bulk counterparts. This review begins by discussing the core principles that govern the unique characteristics of high entropy alloys. The central portion of the review focuses on the latest methodologies for synthesizing nanoscale high entropy alloys and briefly tabulates the catalytic performance of these materials. In the concluding section, we examine the recent studies on the formation mechanisms of high entropy alloy nanoparticles, with a particular focus on wet-chemistry synthesis methods conducted under mild conditions. We hope this review will help researchers better understand high entropy alloys and high entropy alloy synthesis methods for electrocatalysis.

Introduction

Climate change is a pressing global issue, fueled by growing energy demand and increasing CO_2 emissions.[1] In response, intensive research efforts are being focused on electrochemical technologies such as the hydrogen evolution reaction (HER), oxygen evolution reaction (OER), oxygen reduction reaction (ORR), CO_2 reduction, and ammonia synthesis. These processes offer promising pathways for clean energy storage and sustainable production of essential industrial chemicals. However, 98%[2] of today's hydrogen supply is still produced using carbon-intensive gray hydrogen. Transitioning to green hydrogen and electrochemically synthesized ammonia is therefore crucial not only to cut current CO_2 emissions but also to meet the growing demand for these high-value products across industry, transportation, agriculture, and energy sectors.

Achieving this transition, however, is challenging as there are still several significant issues, one of which stems from electrocatalyst materials, which face several significant limitations that hinder their practical application.

Department of Chemistry, The Waterloo Institute for Nanotechnology, University of Waterloo, Waterloo, Ontario, Canada. E-mail: vmaheshw@uwaterloo.ca

Alexander Li is a master's student at the University of Waterloo. His research focus is on the design of high entropy alloy catalysts for green energy applications such as HER, OER and CO_2 reduction. Alexander received his BSc in Materials and Nanosciences from the University of Waterloo in 2023.

Alexander Li

Nayla Qureshi is an undergraduate student at the University of Waterloo. Her research focus is on the design of photoelectrochemical cells for green energy applications, including HER, OER, and CO_2 reduction. Nayla is currently pursuing her BSc in Materials and Nanosciences at the University of Waterloo.

Nayla Qureshi

1. Reliance on precious metals: A significant drawback of current high-performance catalyst materials is their heavy dependence on precious noble metals such as platinum, gold, and silver. The high cost and limited availability of these metals make them economically impractical and unsustainable for large-scale industrial applications.

2. Suboptimal performance of existing electrocatalysts: the efficiency of current electrocatalysts remains inadequate, contributing to the high cost of green hydrogen production, which ranges from $4–$6 USD per kilogram compared to gray hydrogen's more economical $0.80–$2.70 USD per kilogram.[2] This disparity is primarily due to electricity costs, which account for around 90% of green hydrogen's total production expenditure.[3] To address this challenge, it is crucial to develop advanced catalysts capable of achieving higher efficiencies at higher current densities. While research has showcased promising electrolysis systems with high efficiencies, their industrial counterparts lag significantly behind, highlighting a substantial gap between laboratory success and real-world application.

3. Limited stability: The durability of current catalysts proposed in research falls short of meeting the demands of industrial-scale applications. These catalysts struggle to maintain consistent performance under the challenging conditions of industrial electrolysis systems. For example, they must endure extreme operating environments, including high pH levels of 20–30 wt% KOH (4–7 M),[4] varying temperatures from below 80 °C for transportation applications to over 650 °C for solid oxide electrolyzer cells and high current densities of up to 2 A cm^{-2}.[5] Developing catalysts capable of withstanding these challenges is essential for advancing industrial hydrogen production.

4. Selectivity challenges: Catalysts for CO_2 reduction and ammonia synthesis frequently encounter significant selectivity challenges. In the case of CO_2 reduction, selectivity is often hindered by competition with the hydrogen evolution reaction, as the CO_2-to-CO conversion occurs at a potential of −0.1 V *vs.* standard hydrogen electrode (SHE). For ammonia synthesis, the difficulty stems from the remarkable stability of N_2, requir-

ing substantial energy input to break the triple bond. This demand for high activation energy typically necessitates elevated temperatures and large overpotentials,[6] which further intensifies HER competition. As a result, achieving the desired product often requires additional purification or post-processing steps, increasing production costs.

To address these issues, there has been growing interest in developing electrocatalysts using high entropy alloys (HEAs).[7–14] HEAs are alloys that typically contain five or more elements with atomic ratios falling between 5 and 35%. HEAs were initially discovered by two independent groups around the same time in 2004.[15,16] A prior rationale at the time was that, according to Hume–Rothery rules, the synthesis of this class of material should not be possible. However, Yeh *et al.*[15] found that by introducing more elements into a system, the configurational entropy (ΔS_{conf}) increases. ΔS_{conf} becomes ~1.6 times the gas constant when the system has five elements at equimolar ratios. As a result, when making an alloy of five or more elements, configurational entropy can be greater than the enthalpies of compound formation, thus deterring the formation of intermetallic phases. Additionally, the high configurational entropy inherent in these materials contributes significantly to their thermodynamic stability. This entropy effect reduces the Gibbs free energy, making the resulting material inherently stable. With about 60 usable elements in the periodic table, the number of possible new, equiatomic, five-element HEAs exceeds five million. Therefore, HEAs are very interesting for catalytic applications due to the unique heterogeneous surfaces created by the diverse elemental combinations. As a result of the random distribution of elements across the surface and throughout, HEA materials possess significant lattice distortion, creating unique local electronic structures. Additionally, the potential diversity of neighboring elements introduces numerous synergistic effects, which enhance the material's ability to optimize adsorbate interactions and stabilize reaction intermediates. With the vast space of possible combinations, HEAs offer the potential of finding catalysts with specific synergistic effects tailored for improving the performance of various electrochemical processes. Due to all these effects, there has been a surge of interest in using HEAs in electrocatalysis. HEAs have already demonstrated superior stability and performance compared to traditional multielement catalysts for HER, OER, ORR, HOR, and CO_2 reduction reactions. The focus of this review is on the synthesis methods for HEAs that use mild conditions, and the challenges associated with their formation and characterization. The key electrochemical parameters of HEAs for HER, OER, ORR, CO_2 reduction, and ammonia synthesis are tabulated in the review to illustrate their performance.

Vivek Maheshwari is an associate professor of chemistry at the University of Waterloo. He is also a member of the Waterloo Institute for Nanotechnology. His group's research interests include development of nanomaterials for electrocatalysis, lead halide perovskite materials for devices and sensors, and 1D materials for wearable devices. He completed his bachelor's degree from the Indian Institute of Technology, Delhi, and his doctorate from Virginia Tech.

Vivek Maheshwari

Core effects in high entropy alloys

High entropy effect

The high entropy effect, originally proposed by Yeh *et al.*,[15] is fundamental to understanding the formation of HEAs. This

effect arises primarily because, as more elements in equiatomic ratios are introduced into a system, the mixing entropy of the system increases. The relationship describing this increase is shown below, where n represents the number of elements, and R is the gas constant.

$$\Delta S_{\mathrm{mix}} = -R \ln(n) \tag{1}$$

In mixtures containing 3, 5, 6, 9, and 13 elements, the configurational entropy values are observed to be $1.10R$, $1.61R$, $1.79R$, $2.20R$, and $2.57R$, respectively.[15] Yeh and colleagues proposed that the mixing entropy in multi-component systems is substantial enough to drive the Gibbs free energy of mixing (ΔG_{mix}) to a favorable level, effectively overcoming the Gibbs free energy associated with intermetallic formation ($\Delta G_{\mathrm{inter}}$). The high entropy effect has been demonstrated in multiple studies. For instance, in an X-ray diffraction (XRD) investigation by Tsai *et al.*,[8] researchers systematically increased the number of elements in the alloy, progressing from a binary to a septenary system, while observing phase transformations *via* XRD (Fig. 1).

The results revealed that, despite the increasing complexity, the phases in quinary, senary, and septenary alloys remain unexpectedly straightforward, primarily forming two major phases with simple body-centered cubic (BCC) and face-centered cubic (FCC) structures. However, it should be noted that the septenary alloy included minor intermetallic phases that were not observable in the XRD data. This simplicity in structure challenges conventional expectations that increasing component complexity would lead to a plethora of binary and ternary compounds.

It is essential to recognize, however, that the high entropy effect alone does not guarantee the formation of a solid solution phase. Numerous studies report the emergence of intermetallics upon the addition of certain elements. Ultimately, the formation of HEAs is governed by the competition between the entropy of mixing and the enthalpy of intermetallic formation.[17–21] This balance dictates whether a stable solid solution or intermetallic phases will dominate in the alloy.

Lattice distortion effect

Although HEAs typically form in either FCC or BCC phases, the lattice is subject to severe distortion because of the size mismatch among constituent atoms (Scheme 1). The lattice distortion results in important structural properties and a highly localized electronic structure that sets HEAs apart from traditional alloys. The severe lattice distortion hinders dislocation movement, resulting in remarkable mechanical strength. More importantly, in catalytic applications, this distortion profoundly impacts the electronic structure of these materials. The lattice distortion also enhances stability by reducing atomic diffusion, which in turn improves corrosion resistance and may prevent surface reconstruction, further contributing to the material's long-term performance. However, more in-depth surface studies need to be completed to fully evaluate the stability benefit of the lattice distortion effect in nanoscale HEA systems.

Sluggish diffusion effect

During the initial discovery of HEAs, it was surmised that due to the lattice deformation inherent in HEAs, it would potentially result in sluggish diffusion compared to conventional metal alloys.[15] Tsai *et al.*'s[23] early diffusion experiments on FCC Co–Cr–Fe–Mn–Ni alloys demonstrated notably lower diffusion rates than those observed in pure FCC metals and Fe–Cr–Ni(–Si) alloys.

To further analyze this phenomenon, Tsai applied a seven-bond model to calculate local energy fluctuations impacting diffusion. This model revealed that the average potential energy difference between lattice sites in Co–Cr–Fe–Mn–Ni alloys is 50% higher than in Fe–Cr–Ni alloys (Fig. 2). As a result, occupation times in lower-energy sites are approximately 1.73 times greater than in higher-energy sites.[23] This
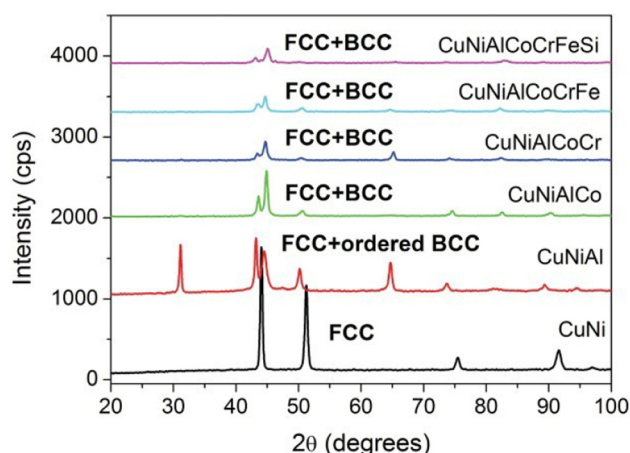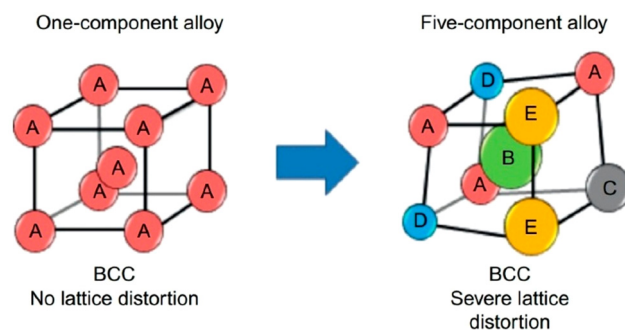

Fig. 1 The XRD patterns of a series of alloys starting from the standard low entropy to mid entropy and eventually to high entropy alloy *via* sequential elemental addition. All the alloys have one or two major phases that have simple structures. Reproduced under terms of the CC-BY license.[8] Copyright (2014), M.-H. Tsai, J.-W. Yeh, published by Taylor & Francis.

Scheme 1 Example of BCC lattice distortion present in high entropy alloys compared to traditional alloys. Reproduced under terms of the CC-BY license.[22] Copyright (2019), W. Dong, Z. Zhou, M. Zhang, Y. Ma, P. Yu, P. K. Liaw, G. Li, published by MDPI.
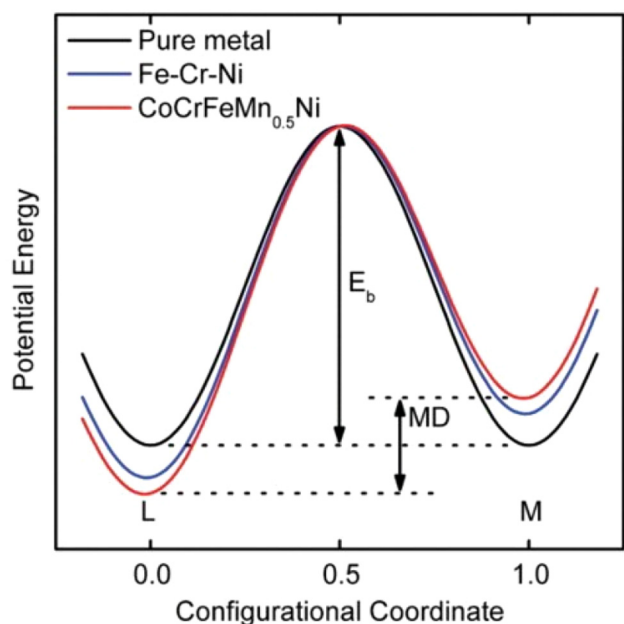
Fig. 2 A potential energy plot illustrating the energy variation during the migration of a Ni atom. In pure metals, the mean difference (MD) in potential energy after each migration is zero, whereas HEAs exhibit the largest energy fluctuation. Reproduced from ref. 23 Copyright (2013), with permission from Elsevier.

extended occupation contributes to the slower overall diffusion in HEAs.

Following the initial study, numerous recent investigations have sought to explore this effect in greater detail. Wang *et al.*[24] conducted an insightful study employing HEA sandwiches with varying atomic ratios of FCC CoCrCuFeNi HEAs.

This approach allowed for the precise measurement of diffusion within individual layers and across the interfaces between HEA layers (Scheme 2). By utilizing these varied atomic ratios, concentration gradients were generated at the interfaces, facilitating the study of diffusion behavior. Their results highlighted a notable finding: sluggish diffusion was observed exclusively at the layer interfaces, while diffusion within the layers themselves did not exhibit sluggish character-

Scheme 2 Prepared HEA sandwiches, with varying HEA compositions at various locations within the structure. Reproduced from ref. 24 Copyright (2018), with permission from Elsevier.

istics. Additional studies indicate that diffusion in HEAs does not correlate with factors like configurational entropy or potential energy fluctuations, suggesting that the sluggish diffusion characteristics may not be intrinsic to HEAs but instead emerge from complex interactions among various elements.[20,21,25–27] Consequently, sluggish diffusion cannot be assumed for every HEA combination. Nevertheless, sluggish diffusion has often been cited as a key factor contributing to the enhanced stability and corrosion resistance of nanoscale HEA catalysts.[28] One approach researchers have used to demonstrate sluggish diffusion is through capturing transmission electron microscopy (TEM) images of HEA nanoparticles after stability testing. These studies have shown that HEAs exhibit reduced or limited *in situ* surface reconstruction compared to traditional platinum-on-carbon counterparts. HEAs have also demonstrated minimal surface reconstruction even under more challenging conditions such as increased overpotentials, high current densities, and varying electrolyte concentrations.[29–38] However, a more thorough investigation is required to determine whether the sluggish diffusion effect is the cause of reduced surface reconstruction in HEA-based electrocatalysts.
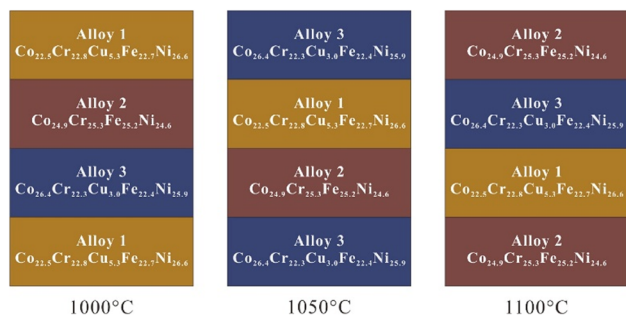
Cocktail effect

The "cocktail effect" in HEAs refers to the synergistic benefits that arise from combining multiple elements in nearly equal proportions. This complex mixture of elements leads to a wide range of interactions that often enhance material properties, such as mechanical strength, corrosion resistance, thermal stability, and catalytic performance, that are difficult or impossible to achieve in simpler alloys. These improvements stem from the intricate interplay between varying atomic sizes, electronic configurations, and bonding characteristics, often resulting in phenomena like lattice distortion, enhanced solid-solution strengthening, and superior overall performance. However, the complexity of the cocktail effect also makes it challenging to predict the impact of compositional changes or the addition of new elements. Simply adding an element based on its bulk properties does not guarantee an improvement, as the overall behavior of the alloy depends on the interactions between all its constituents.

High entropy alloy formation and phase design

Empirical parameters/design guidelines for solid solution HEAs

Although much of the research on HEAs still relies on trial and error, several empirical rules have emerged that offer broad guidelines for predicting their formation.[7,39] Notably, HEAs generally follow modified versions of the Hume–Rothery rules, with additional empirical criteria developed as extensions of these principles.[39] These rules are as follows:

1. ΔS_{mix} should be maximized, and typically, HEAs are classified as alloys with ΔS_{mix} greater than or equal to 1.5R.

Alloys with entropies below $1.5R$ and greater than $1R$ are typically considered mid-entropy alloys. However, it should be noted that HEAs are not materials with maximized entropy, as metallic glasses and high-entropy metallic glasses can exhibit even greater entropy. The equation for ΔS_{mix} is listed below.

$$\Delta S_{\mathrm{mix}} = -R \sum_{i=1}^{N} c_i \ln c_i \qquad (2)$$

where R is the ideal gas constant, N is the number of component elements and c_i is the atomic fraction of ith component element.

2. Mixing enthalpy (ΔH_{mix}) should be greater than -15 kJ mol^{-1} and less than 5 kJ mol^{-1}.[40] As values outside these ranges can result in intermediate phases/intermetallics. ΔH_{mix} is given by the following equation:

$$\Delta H_{\mathrm{mix}} = \sum_{i=1,i \neq j}^{N} 4\Delta H_{ij}^{\mathrm{mix}} c_i c_j \qquad (3)$$

The binary mixing enthalpy is given as $\Delta H_{ij}^{\mathrm{mix}}$ between the ith and the jth elements. While c_i and c_j are the respective atomic fractions of the ith and j^{th} elements.

3. Both earlier thermodynamic parameters of ΔH_{mix} and ΔS_{mix} can be combined to form Ω, a unitless parameter, denoted by the following equation:[41]

$$\Omega = \frac{T_{\mathrm{m}} \Delta S_{\mathrm{mix}}}{\Delta H_{\mathrm{mix}}} \qquad (4)$$

where T_{m} is the melting temperature using the rule of mixtures, denoted by the equation:

$$T_{\mathrm{m}} = \sum_{i=1}^{n} c_i T_i \qquad (5)$$

where T_i is the melting temperature of the ith element in the system. c_i is the atomic fraction of ith component element. Ω should be greater than 1.1 to promote solid solution formation.

4. The atomic radii of the component elements of an HEA should be similar to form a solid solution phase. Zhang et al.,[40] therefore proposed a parameter, δ, representing the average lattice mismatch of the constituent elements. The maximum lattice mismatch must be below 6.6% otherwise phase separation or intermetallic formation could occur. The following equation denotes the average lattice mismatch:

$$\delta = \sqrt{\sum_{i=1}^{N} c_i \left(1 - \frac{r_i}{\bar{r}_{\mathrm{avg}}}\right)^2} \qquad (6)$$

$$\bar{r}_{\mathrm{avg}} = \sum c_i r_i \qquad (7)$$

where r_i is the atomic radii of the ith element while $\bar{r}_{\mathrm{avg}}$ is the weighted average atomic radii of all elements in the HEA composition. c_i is the atomic fraction of ith component element.

5. Valence electron concentration (VEC) is a valuable predictor of crystal phase and stability in HEAs.[42] When VEC exceeds

8, the formation of an FCC phase is likely. For VEC values between 6.87 and 8, a mixed BCC-FCC phase may be observed. Finally, if VEC falls below 6.87, BCC phase is more likely to form. However, it should be noted that certain HEA compositions containing Mn deviate from the expected trends predicted by VEC calculations.[42]

$$\mathrm{VEC} = \sum c_i \mathrm{VEC}_i \qquad (8)$$

VEC_i is the valence electron concentration of ith component element, while c_i denotes the atomic fraction of ith component element.

6. The constituent elements in an HEA composition should have similar electronegativities.[43,44] Significant electronegativity differences can promote the formation of intermetallic compounds, destabilizing the phase and inhibiting the formation of a single solid-solution phase. While no universally accepted threshold exists for determining solid-solution formation, minimizing electronegativity differences χ is generally recommended to enhance phase stability.

$$\chi = \sqrt{\sum c_i \left(1 - \frac{\chi_i}{\chi_{\mathrm{avg}}}\right)^2} \qquad (9)$$

$$\chi_{\mathrm{avg}} = \sum c_i \chi_i \qquad (10)$$

χ is the difference in electronegativity of the constituent elements. χ_i is the electronegativity of the ith component element. χ_{avg} is the weighted average electronegativity of all constituent elements. c_i is the atomic fraction of ith component element.

7. Ye et al.[45] proposed the parameter ϕ to account for the effects of dense atomic packing and atomic size mismatch, which influence the enthalpy of formation and can lead to excessive ΔS_{mix}. They identified a critical ϕ value of 20 as the boundary between single-phase and multi-phase HEA formation: Values below 20 generally yield multi-phase HEAs, whereas values above 20 typically yield single-phase HEAs.

$$\phi = \frac{S_{\mathrm{C}} - S_{\mathrm{H}}}{|S_{\mathrm{E}}|} \qquad (11)$$

where S_{C} is the configurational entropy of mixing for an ideal gas and S_{E} is the excessive entropy of mixing that is a function of atomic packing and atom size.[46] S_{H} or complementary entropy can calculated below using eqn (3) and (5) below:

$$S_{\mathrm{H}} = \frac{\Delta H_{\mathrm{mix}}}{T_{\mathrm{m}}} \qquad (12)$$

8. Λ, a geometric parameter proposed by Singh et al.,[47] combines thermodynamic and geometric considerations to predict phase formation in HEAs. Λ values over 0.96 predict single-phase HEA formation, values between 0.96 and 0.24 predict multi-phase formation, and values below 0.24 predict the formation of intermetallic compounds.

$$\Lambda = \frac{\Delta S_{\mathrm{mix}}}{\delta^2} \qquad (13)$$

Λ can be calculated using parameters from eqn (2) and (6).

9. Wang *et al.*[48] proposed a parameter, γ, to more accurately account for atomic packing misfit compared to conventional atomic size mismatch calculations. Their analysis showed that the primary contributions to atomic packing misfit can be effectively simplified by considering the solid angles of atomic packing for the largest and smallest constituent atoms. A critical value of 1.175 was identified, where values below this threshold favored the formation of stable solid-solution phases. In contrast, values above 1.175 tended to produce intermetallic compounds or metallic glasses.

$$\gamma = \frac{\omega_s}{\omega_L} \tag{14}$$

γ is the ratio between ω_s (solid angle of the smallest atom) and ω_L (solid angle of the largest atom).

$$\omega_s = 1 - \sqrt{\frac{\left(r_S + \bar{r}_{avg}\right)^2 - \bar{r}_{avg}^2}{\left(r_S + \bar{r}_{avg}\right)^2}} \tag{15}$$

$$\omega_L = 1 - \sqrt{\frac{\left(r_L + \bar{r}_{avg}\right)^2 - \bar{r}_{avg}^2}{\left(r_L + \bar{r}_{avg}\right)^2}} \tag{16}$$

$\bar{r}_{avg}$ is the weighted average atomic radii of all elements in the HEA composition, calculated using eqn (7). r_S and r_L represent the atomic radii for the smallest and largest atoms in the HEA composition, respectively.

The above-mentioned empirical rules serve as a general guideline for HEA composition selection. However, it should be noted that simply following the rules mentioned above will not guarantee HEA formation for a given elemental composition. Additionally, there is still much debate regarding the definition and classification of HEAs. Therefore, the empirical guidelines for HEA formation are still undergoing ongoing research, which can be read in more detail in the following review papers.[7,39,49,50]

High entropy alloy phase selection beyond empirical rules

Even after successful HEA phase formation, there are still numerous factors that influence the final microstructure and crystal structure of a given composition. Effects such as lattice strain, itinerant electron concentration, processing, and synthesis conditions critically affect the final microstructure and crystal structure of HEAs.

Hume–Rothery VEC calculations alone are insufficient to fully predict the final crystal phases of HEAs. Numerous studies have sought to improve phase prediction by incorporating additional thermodynamic and computational approaches. For example, Caraballo *et al.*[51] investigated the role of lattice strain, analyzing both interatomic spacing mismatch (s_m) and bulk modulus mismatch (k_m). Their method not only enabled more accurate predictions of HEA phase formation but also successfully distinguished between FCC and BCC structures. A single solid-solution phase formation is predicted to occur when $s_m < 1$ and $k_m < 8$. More importantly, they identified a critical k_m of 4. Where $k_m < 4$ predicts FCC formation, while $4 < k_m < 8$ predicts BCC formation.

Another notable extension of Hume–Rothery approach was presented by Poletti *et al.*,[52] who combined itinerant electron concentration with VEC to refine phase predictions. Their analysis revealed that, consistent with previous observations, lower VEC values generally correspond to BCC formation, while higher VEC values favor FCC. Furthermore, they found that high itinerant electron concentrations, particularly when coupled with low VEC, also promote BCC formation (Fig. 3).

Aside from general phase predictions, active research has been directed towards the development of phase diagrams for HEAs. Like conventional metals and alloys, HEAs can undergo crystal phase transitions or form mixed-phase structures through composition tuning, mechanical stress, or temperature variations during synthesis and annealing. Their behavior often parallels that of traditional alloy systems described by phase diagrams. However, the high compositional complexity of HEAs means that comprehensive phase diagrams are still under development.[53–58]

Like traditional metals and alloys, HEAs have also demonstrated polymorphism. Notably, Zhang *et al.*[59] were the first to report polymorphism in HEAs by applying hydrostatic compression to the FCC CoCrFeMnNi Cantor alloy at room temperature, inducing a phase transition from FCC to HCP. However, it should be noted that to achieve the phase transition, a pressure of ~41Gpa was needed, which can only be achieved using a diamond anvil cell.

Temperature effects on HEA formation remains an area of active research. The temperatures used during synthesis and annealing significantly affect not only phase formation but also the resulting crystal structure and phase purity of HEAs. In addition to temperature, cooling rate has been found to play a critical role in determining crystal phase composition
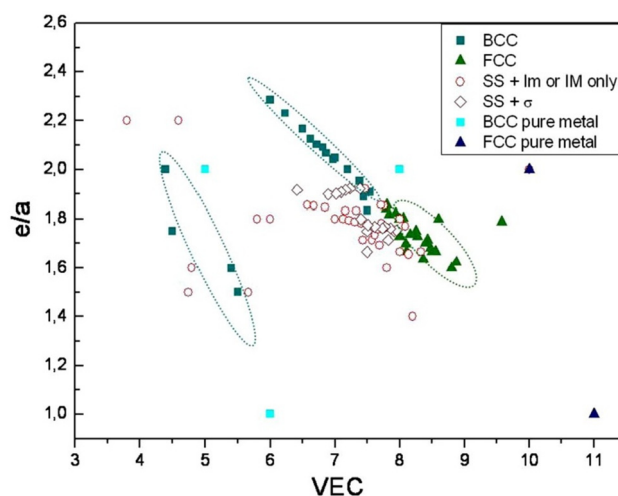

Fig. 3 VEC and itinerant electron (e/a) plot of various multielement systems. Highlighted correlation of lower VEC and high e/a predicts BCC phase formation. Reproduced from ref. 52 Copyright (2014), with permission from Elsevier.

and HEA formation. For example, $Al_{0.5}CoCrFeNi$ has been reported to form either FCC + BCC or FCC + BCC + B2 phases depending on the cooling rate.[60] However, careful consideration must be given to cooling conditions, as it is generally observed that rapid cooling suppresses the formation of intermetallic compounds and promotes the retention of solid solution phase.

In summary, the formation and stability of crystal phases in HEAs are not governed solely by composition. They are also heavily influenced by processing and synthesis conditions, including temperature, mechanical stress, and cooling rate. These factors can induce phase transitions, polymorphism, and the emergence of mixed-phase structures, even in systems with identical elemental compositions. As comprehensive phase diagrams for HEAs are still in development, understanding the interplay between thermodynamics and kinetics remains essential. Fine-tuning these conditions provides a powerful approach for tailoring the structural and catalytic properties of HEAs.

Catalytic advantages of nanoscale high-entropy alloys

Corrosion resistance

The corrosion properties of HEAs are particularly of interest for their industrial applications in catalytic systems. It directly impacts the operational lifespan of catalysts, which typically require periodic replacement due to degradation. Catalysts with higher corrosion resistance are better equipped to withstand the harsh operating conditions often encountered in industrial-scale electrolyzers and other demanding environments. Early findings suggest that HEAs generally offer superior corrosion resistance compared to traditional alloys.[61] This has been demonstrated in various electrochemical applications, where HEAs show increased stability in concentrated acidic and basic electrolytes. HEAs, like traditional alloys, can improve corrosion resistance by incorporating elements known for forming protective passivation layers, such as chromium or aluminum. However, the underlying corrosion behavior of HEAs is complex and not solely dependent on increasing the content of corrosion-resistant elements.[62,63] Due to the unique multi-element nature of HEAs, their corrosion properties are also influenced by synergistic interactions between the elements, which are still not fully understood.[64]

Early work by Lee et al.[65] investigated the effect of aluminum content on the corrosion behavior of $Al_xCrFe_{1.5}MnNi_{0.5}$ in 0.5 M H_2SO_4. In H_2SO_4, aluminum typically forms an Al_2O_3-rich passive layer. However, this layer is known to be porous and non-uniform, allowing continued ingress of H^+ ions and subsequent localized attack beneath the oxide film. Tests showed the corrosion potential (E_{Corr}) decreased, while both the corrosion current (I_{corr}) and the passivation current (I_{pass}) increased as the aluminum content increased. Further electrochemical impedance spectroscopy (EIS) tests confirmed this by showing a decrease in charge transfer resistance (Fig. 4a and b).
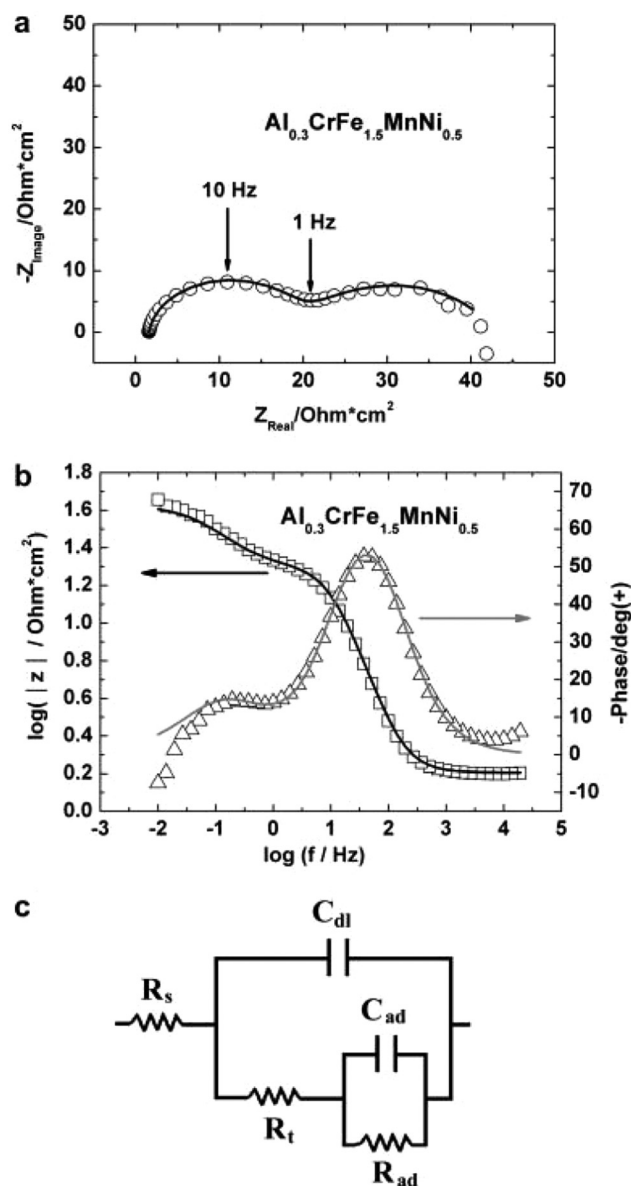

Fig. 4 EIS results for $CrFe_{1.5}MnNi_{0.5}$ alloy in 0.5 M H_2SO_4 solution. Nyquist (a) and Bode (b) plots along with (c) equivalent electrical circuit. Scattered points represent raw experimental data points, and solid lines represent model fit. Reproduced from ref. 65 Copyright (2008), with permission from Elsevier.

Interestingly, a second capacitive loop was observed during EIS measurements (Fig. 4c), highlighting the presence of an adsorbed layer and charge transfer processes at the metal–electrolyte interface. The adsorptive complexes on the interface were a result of Al dissolution by the following mechanism:

$$Al_{(s)} + H_2O \rightarrow Al(OH)_{ad} + H^+ + e^- \quad (17)$$

$$Al(OH)_{ad} + 5H_2O + H^+ \rightarrow Al^{3+} + 6H_2O + 2e^- \quad (18)$$
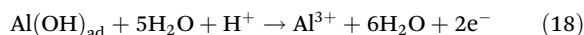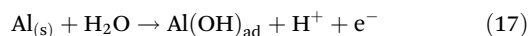
Another HEA composition, $Al_xCoCrFeNi$, was also tested in the same environment, and comparable results were observed. Increasing the aluminum content led to decreased corrosion

resistance. While the observed trends align with conventional understanding of aluminum corrosion in acidic media, it should be noted that as the aluminum content increased, the corrosion resistance decreased. The decrease in corrosion resistance is primarily attributed to increased oxide layer porosity and changes in crystal structure. Although the oxide layer becomes thicker with higher aluminum content in the HEA, it also becomes more porous, allowing greater ingress of H^+ ions and thus accelerating corrosion. Additionally, the increased aluminum content induces a phase transition in the alloy, shifting from a mixed FCC/BCC structure to a predominantly BCC phase. Therefore, changes in elemental composition and the resulting changes in crystal structure must be carefully considered. Both the crystal structure and surface behavior play a critical role in determining the corrosion behavior of high entropy alloys.

Another crucial factor that can increase corrosion is galvanic corrosion at the interfaces between mixed-phase HEAs. Ren et al.[66] investigated the corrosion behavior of copper additions in a $Cu_xCrFeNiMn$ HEA composition tested in 1 M H_2SO_4.

Both Cu and Cr play significant roles in corrosion resistance. Cr forms a passivation layer, enhancing corrosion resistance, while Cu promotes the formation of single FCC phases, reducing galvanic corrosion. However, as Cu content increases, inter-dendritic (ID) FCC + BCC phases begin to form (Fig. 5a and b). This results in Cu-rich, Cr-depleted zones alongside Cr-rich, Cu-depleted zones, leading to galvanic corrosion between the ID and dendrite-rich regions (Fig. 5b).

When designing a HEA catalyst, it is essential to thoughtfully select the alloying elements, as the electrolyte conditions significantly impact stability and performance requirements. In acidic environments, such as those involving electrolytes like H_2SO_4, protective passivation films can degrade rapidly, leading to accelerated oxidation and metal dissolution. Conversely, in alkaline environments, using electrolytes like KOH, corrosion rates may decrease due to the formation of protective oxide layers. However, these oxide layers, while reducing corrosion, may not always enhance catalytic performance and could even hinder it, depending on the specific application. Mixed-phase HEAs, in particular, warrant closer investigation due to their susceptibility to galvanic corrosion at phase interfaces, which can compromise their corrosion stability.[61,62,65] Consequently, both phase uniformity and the potential galvanic corrosion between the catalyst and the catalyst support should be carefully evaluated to optimize corrosion resistance. Additionally, passivation films formed by elements such as Cr and Al can affect catalytic performance by altering the active site area/properties, which must be considered in the design process.

Effect of crystal phase and crystal planes on electrocatalytic performance in High entropy alloys

Crystal lattice engineering has been widely used to enhance the catalytic performance of conventional metals and metal alloys. In traditional catalyst systems, several strategies are
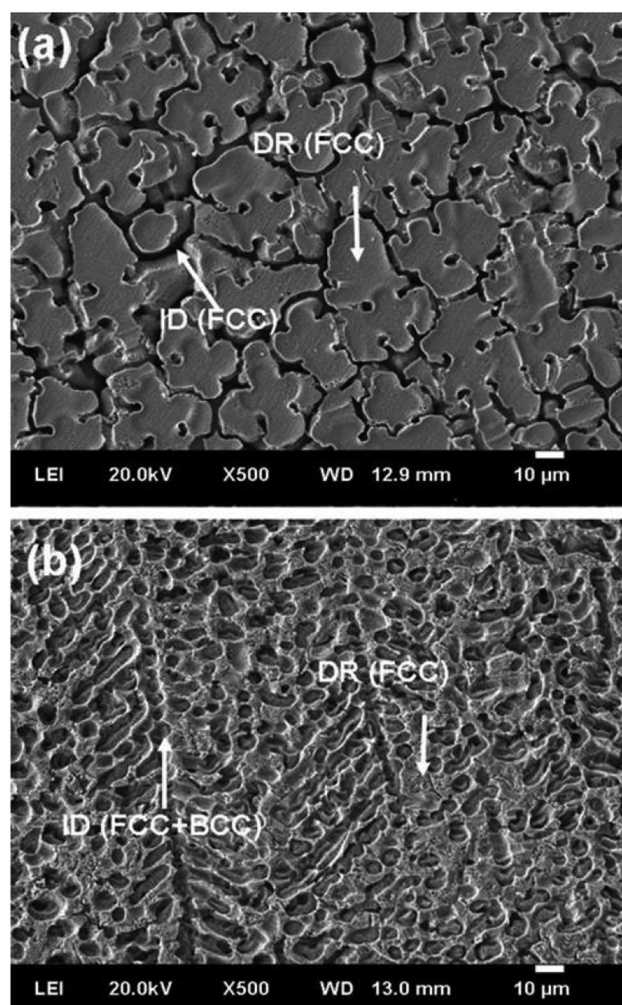

Fig. 5 Scanning electron microscope (SEM) images of CuCrFeNiMn alloy systems: (a) $CuCr_2Fe_2Ni_2Mn_2$, (b) $Cu_2CrFe_2NiMn_2$. Reproduced from ref. 66 Copyright (2011), with permission from Wiley.

employed to control catalytic behavior, with the most common being strain engineering, crystal phase control, and crystal facet engineering.

For many transition metal-based catalysts, activity is closely tied to the filling of bonding and antibonding states within the d-band. Pt, a benchmark catalyst for HER, has been alloyed with various metals to adjust its lattice parameters. When alloyed with elements of varying atomic sizes, compressive or tensile strain can be introduced into the platinum lattice. This strain shifts the d-band center, improving adsorption and desorption properties and thus enhancing catalytic performance. However, applying these same principles to HEAs introduces significant complexity. In these multicomponent systems, lattice parameters can often be approximated using Vegard's law, which estimates the effective lattice constant as a weighted average of the constituent elements. Maruta et al.[67] demonstrated that lattice parameters predicted by Vegard's law show good linear correlation with experi-
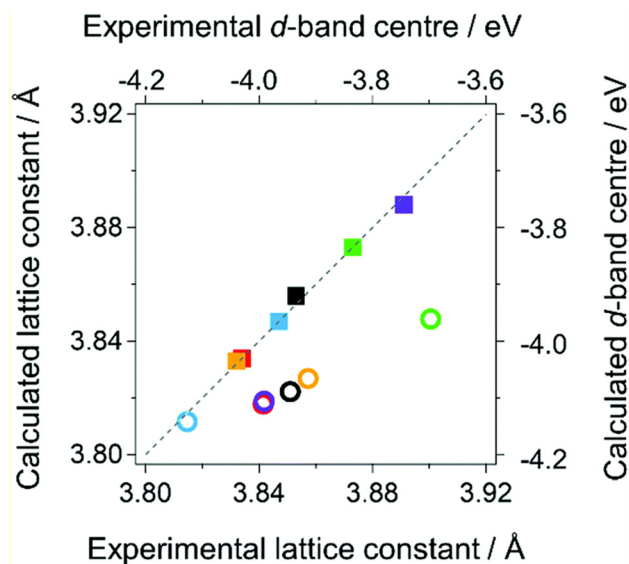
Fig. 6 Plot of calculated and measured lattice constants as well as d-band centres. Linear correlation is observed between calculated and measured lattice constants. Reproduced from ref. 67 Copyright (2022), with permission from RSC publishing.

Fig. 7 (a) Overpotential of various HEA composition at 50 mA cm^{-2}. (b) Turn over frequency compared with d-band centre. Reproduced from ref. 67 Copyright (2022), with permission from RSC publishing.

mentally measured values across a range of HEA compositions (Fig. 6).

In addition to structural measurements, Maruta *et al.* also investigated the d-band electronic structure of various HEAs. Their results revealed a lack of correlation between theoretically calculated and experimentally measured d-band centers (Fig. 6). More importantly, the position of the d-band center did not correlate with HER activity in HEAs (Fig. 7a and b). This suggests that factors beyond bulk electronic structure, such as local atomic environments, orbital hybridization, or synergistic ("cocktail") effects, may play a more dominant role in determining catalytic behavior. Furthermore, recent studies challenge the assumption that HEAs are entirely random solid solutions. Evidence now shows that HEAs can exhibit both long-range disorder and short-range chemical ordering, which can significantly influence their structural stability and catalytic performance.[68]

Crystal phase control has been extensively utilized as a strategy to enhance the catalytic and structural properties of metal and metal alloy-based catalysts. Phase transitions alter atomic packing and surface site symmetry, which in turn can dramatically affect electronic structure. In some cases, this enables catalysis in materials previously considered inert or drastically improves catalytic performance. For instance, Liu *et al.*[69] synthesized a metastable HCP layer of Pt on nickel nanocrystals, resulting in a significant enhancement in mass activity for alkaline HER. Despite the potential performance advantages, the role of the crystal phase in HEA-based electrocatalysts remains largely underexplored. Studies have reported enhanced catalytic activity in both single-phase and dual-phase HEAs.[70,71] However, achieving controlled phase transitions in HEAs often requires compositional tuning, making
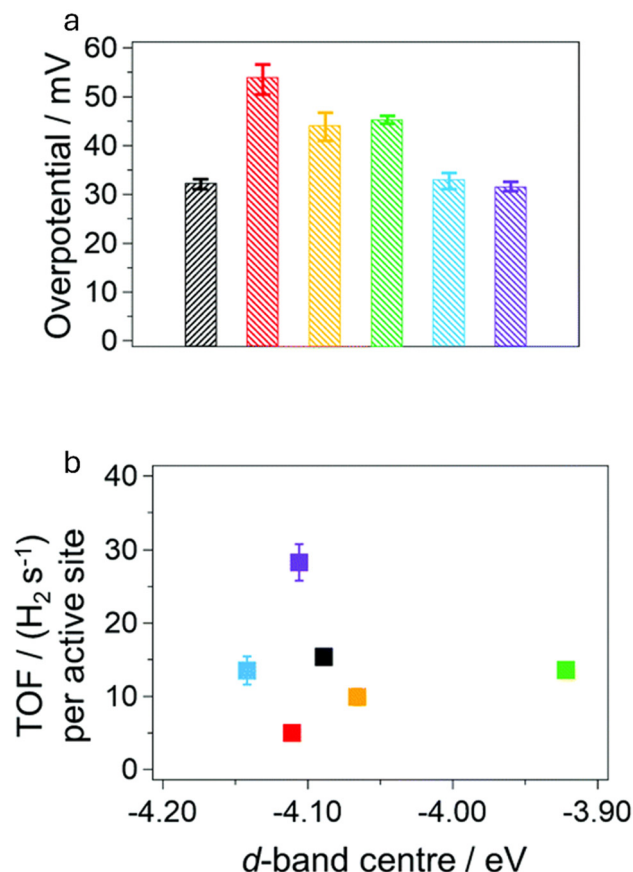
it challenging to isolate the effect of crystal structure on catalytic performance. As a result, more systematic investigations are needed to clarify the influence of the crystal phase on electrocatalytic behavior in HEAs.

Another powerful strategy to enhance catalytic performance is facet engineering. For the HER, Pt has been widely studied, with different crystal facets (*e.g.*, Pt(111), Pt(100)) known to exhibit distinct hydrogen binding energies.[72] More recently, edge sites have been identified as even more catalytically active, prompting efforts to design nanostructures that expose these high-index sites to maximize activity and Pt utilization.[73] In contrast, most HEA catalysts synthesized to date are limited to simple spherical morphologies, with few methods available to fabricate nanostructures with well-defined or complex geometries.[74–76] Recently, Hsiao *et al.*[76] synthesized HEAs with different facets by utilizing cubic and octahedral Pd seeds with {100} facets and {111} facets, respectively. It was found that with the same HEA composition, the {100} facets showed significantly better HER and ethanol oxidation reaction (EOR) performance compared to both commercial pt as well as the {111} facets. Highlighting the fact that more catalytic performance can be obtained in HEAs through facet Engineering. Overall, these findings highlight a critical need for the devel-

opment of advanced synthesis techniques capable of producing HEAs with tailored nanostructures and exposed active facets.

In conclusion, while crystal lattice engineering has shown great promise in enhancing the catalytic performance of conventional metals and alloys, its full potential in HEAs remains largely untapped. The inherent complexity of HEAs arising from their multi-element compositions and structural variability poses significant challenges for isolating and understanding lattice-driven effects. To move the field forward, more systematic and targeted studies are urgently needed to unravel the interplay between lattice parameters, crystal phase, and surface structure. Advancing our understanding of these areas will be critical for designing the next generation of HEA-based electrocatalysts.

Density functional theory (DFT) calculations for high-entropy alloys

DFT has been instrumental in predicting and modelling binding behavior for traditional transition-metal-based catalysts. However, applying DFT calculations to HEAs presents substantial challenges in accurately predicting their performance. The inherent complexity of HEAs, arising from their multi-element compositions and disordered atomic structures, renders traditional DFT approaches insufficient for fully capturing their unique behavior. Additionally, the large unit cells required to model HEA surfaces significantly increase computational costs, making precise surface binding predictions with DFT alone impractical.

In conventional transition-metal catalysts, DFT calculations often rely on d-band theory to optimize adsorbate bonding. Experimentally, however, HEAs exhibit electronic structures that differ dramatically from those of conventional alloys. HEAs display a widening of the d-band center rather than a simple shift. Hence, methods for traditional alloys are not applicable for the prediction of HEA properties.

The exceptional catalytic performance of HEAs stems from their diverse local density of states and the variety of coordination sites available on their surfaces. These unique properties enable more optimized binding sites and foster interactions between neighboring atoms, which can stabilize reaction intermediates. This intricate synergy is typically associated with the so-called "cocktail effect" frequently referenced in academic papers and reviews. This intricacy also complicates the DFT based calculations for HEAs. However, finding new parameters for predicting the performance of HEAs and methods to effectively model their behavior will be crucial for screening and selection of HEAs for specific electrochemical applications.

High entropy alloy nanoscale synthesis approaches

Carbothermal shock (CTS)

Yao et al.[77] developed a carbothermal shock synthesis method for creating HEA-NPs, enabling the integration of up to eight

immiscible elements into single-phase solid-solution structures. Key features of the method include its ultrafast thermal shock process (maximum temperature of 2000–3000 K, with cooling rates of ~10^5 K s^{-1}), which prevents phase separation and enables uniform mixing of elements, resulting in nanoparticles with consistent size (~5 nm) and compositional uniformity.

The CTS method is performed in two main steps. First, metal salt precursors are mixed and loaded onto conductive carbon supports, such as carbon nanofibers (CNFs) (Fig. 8a). The material is subjected to a brief but intense thermal shock via Joule heating, achieved by passing a large electrical current through the support material (Fig. 8b). This process rapidly decomposes the metal salt precursors and drives the fusion of metallic elements into single-phase nanoparticles (Fig. 8c). Using this method, PtCoNiFeCu, PtPdCoNiFe, PtCoNiFeCuAu, PtPdCoNiFeCuAu, and PtPdCoNiFeCuAu HEA nanoparticles were synthesized, all displaying uniform mixing and single-phase solid solution (Fig. 8d).

Key parameters influencing the composition and size distribution of the nanoparticles include the defect concentration of the carbon nanofiber (CNF) support, shock duration, and cooling rates. In Yao et al.'s[77] study, the CNF supports were prepared by carbonizing electrospun polyacrylonitrile fibers. Crucially, the carbonization temperature significantly affected the defect concentration in the supports, which in turn influenced particle dispersion. Higher carbonization temperatures
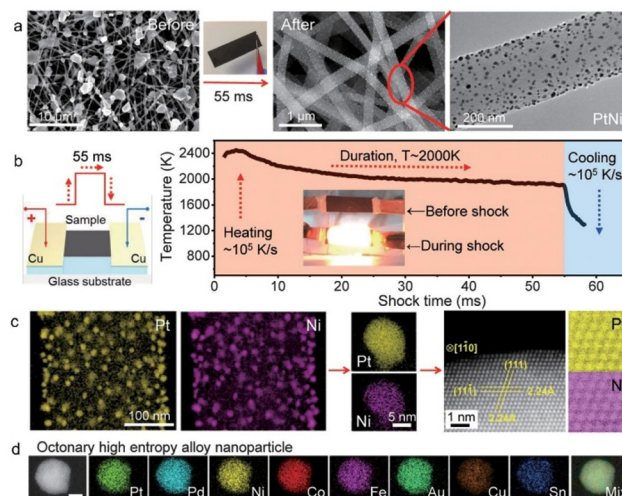

Fig. 8 (a) On left, microscopy images of microsized precursor salt particles on the carbon nanofiber (CNF) support before thermal shock. On right, TEM images of salt loaded CNF after thermal shock resulting in well-dispersed (PtNi) nanoparticles. (b) On left, schematic of the set-up and on right, temperature change during the 55 ms thermal shock. The sample image during the shock is shown in the inset. (c) On left, low-magnification and single-particle elemental maps of PtNi CNF sample. On right, high-angle annular dark-field (HAADF) image, and corresponding atomic maps for a binary PtNi alloy. (d) Individual elemental maps of PtPdNiCoFeAuCuSn HEA-NP, scale bar, 10 nm. Adapted from ref. 77 Copyright (2018), with permission from the American Association for the Advancement of Science.

(*e.g.*, 1273 K) resulted in lower defect concentrations, leading to smaller and more uniform particle distributions. Additionally, shorter shock durations, such as those below 55 ms, produced smaller nanoparticles with tighter size distributions (Fig. 9a and b). The cooling rate is also a key factor to keep in mind for this synthesis method. At slower cooling rates, phase separation becomes evident, disrupting the uniformity of the nanoparticles (Fig. 9c and d). Rapid cooling is, therefore, essential to retaining the high-entropy mixing state and achieving single-phase solid-solution nanoparticles from this method (Fig. 9e). Catalytic testing revealed that HEA-NPs synthesized using this method, particularly quinary PtPdRhRuCe nanoparticles, demonstrated exceptional catalytic activity for ammonia oxidation, achieving ~100% ammonia conversion and >99% nitrogen oxide selectivity at relatively low operating temperatures (700 °C). Operation stability was evaluated for 30 hours of continuous operations, and no signs of degradation were observed.

Despite its remarkable capabilities, the CTS method has certain limitations, primarily its restriction to synthesizing nanoparticle morphologies and its reliance on conductive support materials. This reliance on supports capable of withstanding extreme temperatures and electrical currents without degrading significantly narrows the range of materials that can

be used. Consequently, this limitation restricts the diversity of support–catalyst systems that can be explored, hindering broader investigations into support–catalyst interactions. As an additional consideration, the synthesis of HEAs on carbon support must consider the possibility of carbide formation. Yao *et al.*[77] did not report any carbide formation. Nonetheless, one of the key advantages of CTS is its simplicity and scalability, offering exceptionally high heating and cooling rates, which make it a cost-effective and efficient method for HEA NP synthesis.

Microwave heating

Microwave heating shares similarities with the CTS method in providing rapid and uniform heating. The choice of substrate is critical in microwave heating, as materials must endure high reaction temperatures and efficiently absorb microwaves. Moreover, microwave sources can vary widely, from household microwave ovens to advanced laboratory-grade high-power systems, introducing variability in synthesis outcomes.

Maulana *et al.*[28] utilized microwave heating to synthesize IrFeCoNiCu HEA nanoparticles for acidic OER in 0.1 M HClO$_4$. Metal salt precursors were drop-cast onto carbon paper and subjected to microwave heating for 10–11 seconds at 1200 W. The resulting nanoparticles exhibited a size distribution ranging from 20 nm to 200 nm, with an average size between 20 nm and 50 nm. This broad distribution was primarily attributed to the heterogeneity of the carbon paper substrate and the batch-to-batch inconsistencies due to the household microwave oven used in the process.

Despite these limitations, the synthesized IrFeCoNiCu HEA nanoparticles demonstrated remarkable catalytic performance for OER. The overpotential to achieve 10 mA cm^{-2} was approximately 302 mV, accompanied by a low Tafel slope of 58 mV dec^{-1}. Furthermore, the catalyst's stability was notable, with only a 60 mV increase in overpotential after 12 hours of continuous operation at 10 mA cm^{-2}.

Achieving a narrow size distribution requires careful consideration of the interaction between the microwave source and the substrate. Additionally, similar to CTS, the range of substrates compatible with microwave heating is limited, restricting the scope of catalyst studies that can be conducted using this synthesis method. Furthermore, the use of carbon-based substrates introduces the possibility of carbide formation, which must be carefully considered. However, in the highlighted study, no mention of carbide formation was made.

Ultrasonication-assisted wet chemistry

Miaomiao Liu and colleagues[78] created a novel ultrasonication-assisted wet chemistry method for the synthesis of HEA-NPs. This method exploits the acoustic cavitation phenomenon, where ultrasonic waves generate localized high temperatures (≈5000 °C) and pressures (≈2000 atm) for brief moments, driving rapid and entropy-maximized metal ion reduction. The resulting PtAuPdRhRu HEA-NPs had uniform multi-metallic distributions with average particle sizes of about 3 nm.
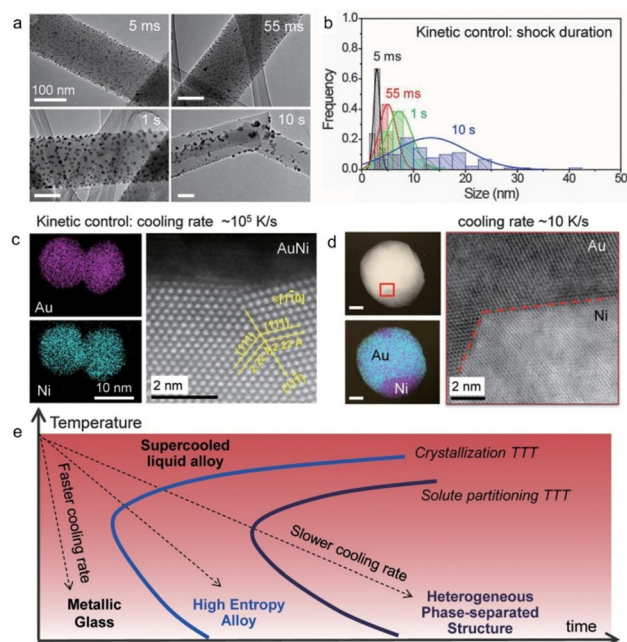

Fig. 9 (a) TEM images (scale bars: 100 nm) of PtNi NPs on CNFs, illustrating the effect of thermal shock duration (5 ms, 55 ms, 1 s, and 10 s) on particle size and dispersity, accompanied by the corresponding size distribution graph (b). (c and d) Elemental maps, HAADF, and annular bright-field (ABF) images (scale bar: 10 nm) of AuNi NPs, highlighting the impact of varying cooling rates. (e) Time–temperature-transformation (TTT) diagram depicting the influence of cooling rate on the kinetic formation of metallic glass, HEA, and phase-separated structures. Adapted from ref. 77 Copyright (2018), with permission from the American Association for the Advancement of Science.

The synthesis process involves dissolving precursor metal salts in ethylene glycol, followed by the addition of X-72 carbon support, a material commonly used with commercially available Pt/C catalysts. The HEA precursor salts were mixed with 10 wt% X-72, calculated relative to the final metallic weight, and then subjected to ultrasonication at 750 watts and 20 kHz under ambient conditions for 10 minutes. Post-sonication, the nanoparticles display a twin-phase structure, with both single and dual-phase FCC peaks observed in XRD analysis.

To achieve a single-phase HEA structure, calcination under N_2 is required. When the calcination temperature is increased from 500 °C to 700 °C, the dual FCC peaks observed in the XRD patterns gradually disappear, resulting in a stable, single-phase alloy structure (Fig. 10a–c). Calcination temperature did not affect the morphology or size distribution of the nanoparticles. PtAuPdRhRu nanoparticles demonstrated excellent performance for HER in 1 M KOH conditions, with an overpotential of 190 mV to reach a current density of 30 mA cm^{-2} and a Tafel slope of 62 mV dec^{-1}. The catalyst maintained stability during continuous operation at 100 mA cm^{-2} for 8 hours.

The method, while innovative, faces some limitations that could be addressed for broader adoption. Access to high-power ultrasonication equipment is a challenge, as such devices are not widely available in many research laboratories. Furthermore, the current approach is not optimized for large-scale applications, making scalability a critical area for improvement.

Fast moving bed pyrolysis

Furnace pyrolysis has been widely utilized for synthesizing metal nanoparticles (NPs). However, a significant limitation of

this technique is the difficulty in achieving the precise heating and cooling rates necessary for more complex NP synthesis. To address this challenge, Gao et al.[79] employed fast-moving bed pyrolysis (FMBP), a method that allows for precise control of heating and cooling rates. This technique involves a mechanical bed that houses precursor materials and can be moved in and out of the heated zone of a tube furnace, enabling rapid and controlled temperature changes (Fig. 11a–c). Furthermore, this method supports the use of granular catalyst supports, unlike CTS.

The versatility of FMBP was demonstrated through the synthesis of various HEA combinations, including a denary (10-element) HEA comprising Mn, Co, Ni, Cu, Rh, Pd, Sn, Ir, Pt, and Au on graphene oxide (Fig. 11d–f). In addition, the method was tested using several support materials, synthesizing CuPdSnPtAu HEA NPs on Al_2O_3, zeolite, carbon black, and graphene oxide.

Temperature effects were also investigated, comparing traditional furnace pyrolysis to FMBP for non-HEA NiPdPt nanoparticles. In traditional pyrolysis, samples required approxi-
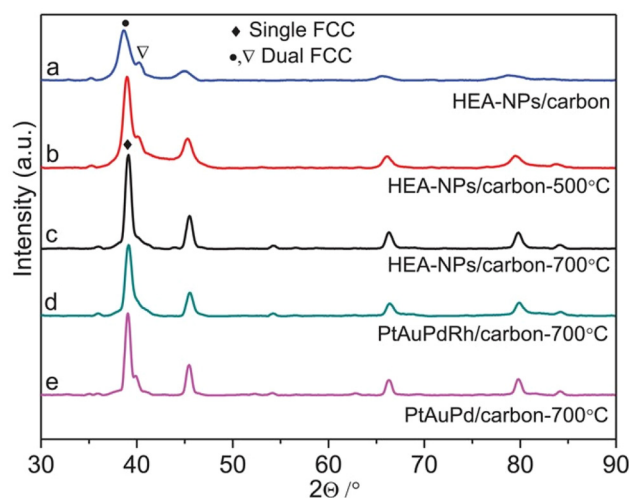

Fig. 11 (a) FMBP experimental setup. (b) HEA-NP synthesis *via* FMBP for homogeneous structures and fixed-bed pyrolysis (FBP) for phase-separated structures. (c) Simulation of the time required for precursors/GO (20 mg, 3 wt%) to reach 923 K during the FMBP process, with the metal precursors/GO positioned in a quartz boat at the center. (d) (Scale bar: 10 nm) HAADF-STEM images of denary (MnCoNiCuRhPdSnIrPtAu) HEA-NPs on GO synthesized *via* FMBP with a 3 wt% loading on GO. (e) (Scale bar: 0.5 nm) HR-STEM image of denary HEA-NPs, with Fourier transform analysis confirming an FCC crystal structure. (f) (Scale bar: 10 nm) Elemental maps of denary HEA-NPs (10 wt% loading on GO), showing an equal atomic ratio of elements. Reproduced under terms of the CC-BY license.[79] Copyright (2020), S. Gao, S. Hao, Z. Huang, Y. Yuan, S. Han, L. Lei, X. Zhang, R. Shahbazian-Yassar, J. Lu, published by Springer Nature.

Fig. 10 XRD patterns of synthesized HEA-NPs/carbon prepared *via* the ultrasonication-assisted wet chemistry method: (a) before calcination under N_2, (b) after calcination under N_2 at 500 °C for 2 hours, and (c) at 700 °C for 2 hours. Additionally, XRD patterns of (d) PtAuPdRh/carbon and (e) PtAuPd/carbon, both synthesized using the same method and calcined under N_2 at 700 °C for 2 hours. Reproduced from ref. 78 Copyright (2022), with permission from Wiley.
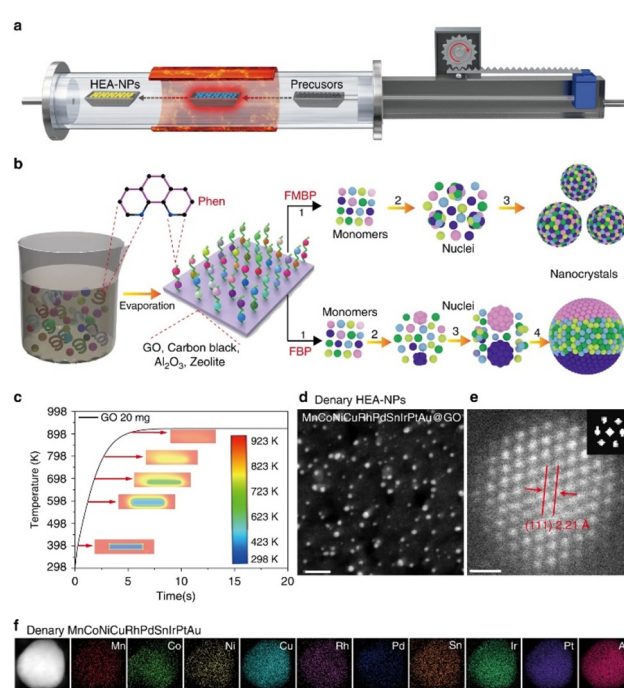
mately 31 minutes to reach 923 K from room temperature, with a heating rate of 20 K min^{-1}. In contrast, FMBP achieved 923 K within 5 seconds. The rapid heating rate of FMBP had a significant effect on phase separation. Traditional furnace pyrolysis yielded phase-separated NiPdPt NPs with a Pd-rich core, whereas FMBP avoided such separation, leading to more uniform nanoparticles (Fig. 11b).

The applicability of the FMBP synthesis method was tested using FeCoPdIrPt HEA NPs as a catalyst for HER. The resulting catalyst demonstrated excellent HER performance, achieving a low overpotential of 42 mV to reach a current density of 10 mA cm^{-2} and a low Tafel slope of 58 mV dec^{-1}. Moreover, the catalyst exhibited outstanding stability, with negligible degradation after 150 hours of continuous operation at 10 mA cm^{-2}.

Solvothermal

Due to the high temperatures and specialized equipment required for top-down synthesis of HEAs, many researchers are increasingly turning to wet chemistry techniques for synthesizing HEA-NPs. Wet chemistry methods allows the production of unique nanostructures with tailored properties. Among these methods, solvothermal synthesis stands out as a straightforward technique that leverages high-boiling-point organic solvents to reach elevated temperatures, eliminating the need for pressure vessels. Solvothermal methods typically involve the use of a reducing agent to simultaneously reduce all metal ions in solution, leading to the formation of HEA NPs. A common solvent for this process is oleylamine, which serves a dual role as both reducing agent and stabilizer for nanoparticles. Additionally, solvothermal methods are compatible with a wide range of conductive supports, making them particularly attractive for catalytic applications.

An excellent demonstration of solvothermal synthesis in HEA catalyst preparation is provided by a study conducted by Chen et al.,[74] where convex cube-shaped Pt$_{34}$Fe$_5$Ni$_{20}$Cu$_{31}$Mo$_9$Ru HEA NPs were synthesized (Fig. 12). Using a one-pot solvothermal method, the researchers combined cetyltrimethylammonium chloride (CTAC), oleylamine, metal acetylacetonates, carbon nanotubes (CNTs), and glucose (Scheme 3). The mixture was heated under stirring at 220 °C for varying reaction durations. The study revealed fascinating insights into the morphology of the nanoparticles: those synthesized with a 1-hour reaction time exhibited a cubic shape (Fig. 12k and i), whereas extending the reaction to 2 hours produced convex cubes. The convex cube nanoparticles, characterized by high-index facets (Fig. 12a–c), demonstrated superior catalytic performance for both HER and OER. Specifically, these nanoparticles achieved remarkably low overpotentials of 10 mV and 259 mV to reach a current density of 10 mA cm^{-2} for HER and OER, respectively, in alkaline conditions (1 M KOH). Furthermore, they exhibited exceptionally low Tafel slopes of 27 mV dec^{-1} for HER and 39 mV dec^{-1} for OER, indicating highly efficient kinetics. The stability of the catalysts was equally impressive, as chronoamperometric testing showed only a 5% decrease in HER current and an 8% decrease in OER current after 40 hours of continuous operation.
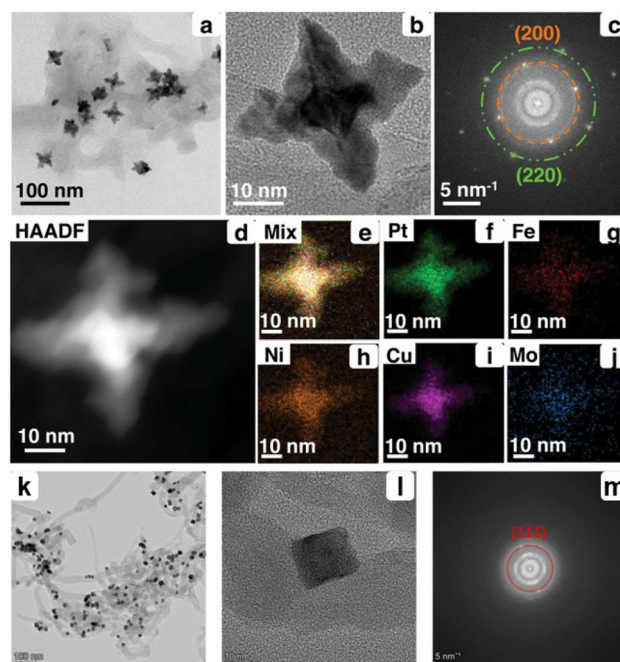

Fig. 12 TEM image of convex cube-shaped Pt$_{34}$Fe$_5$Ni$_{20}$Cu$_{31}$Mo$_9$Ru-2 h at (a) low and (b) high magnification. (c) Fourier transformed electron diffraction pattern of (b). (d) HAADF-TEM image of Pt$_{34}$Fe$_5$Ni$_{20}$Cu$_{31}$Mo$_9$Ru and (e–j) the corresponding elemental mappings. TEM image of Pt$_{34}$Fe$_5$Ni$_{20}$Cu$_{31}$Mo$_9$Ru-1 h at a (k) low and (l) high magnification. (m) Fourier transformed electron diffraction pattern for (l). Adapted from ref. 74 Copyright (2022), with permission from Wiley.
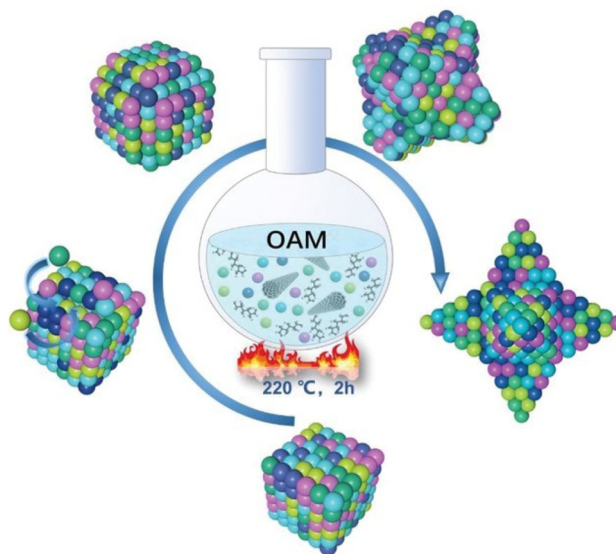
Scheme 3 Schematic of the synthesis of convex cube-shaped Pt$_{34}$Fe$_5$Ni$_{20}$Cu$_{31}$Mo$_9$ HEA on CNT-support. Reproduced from ref. 74 Copyright (2022), with permission from Wiley.

In summary, solvothermal synthesis offers a simple and accessible route to producing HEA NPs with diverse morphologies, while maintaining compatibility with a variety of

conductive supports. However, a notable challenge associated with this method lies in the use of high-boiling-point organic solvents. Residual solvents or organic capping ligands can be difficult to remove and may significantly impact the active surface area of the nanoparticles, thereby affecting their performance in catalytic applications.
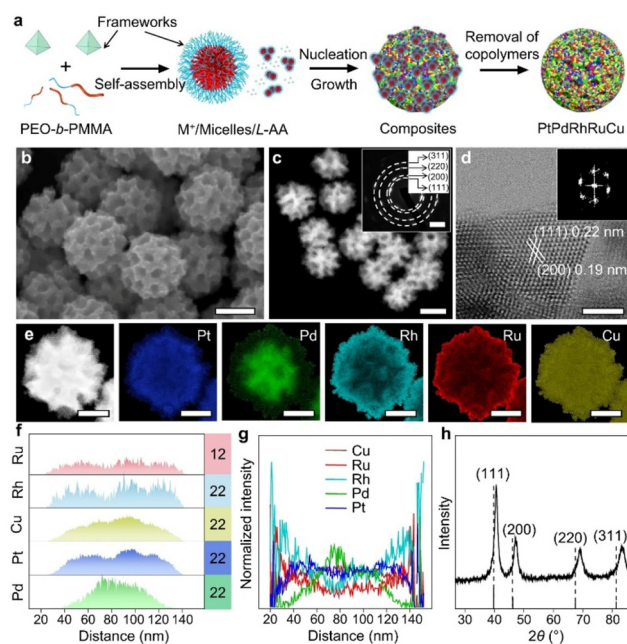

Fig. 13 (a) Synthesis schematic of PtPdRhRuCu Mesoporous multimetallic nanospheres (MMNs). (b) SEM and (c) HAADF−STEM images of PtPdRhRuCu MMNs (scale bar: 100 nm), (c) inset: the corresponding selected area electron diffraction (SAED) pattern (scale bar: 5 nm^{-1}). (d) HRTEM (scale bar: 2 nm) with inset showing Fast Fourier Transform (FFT) patterns. (e) Atomic elemental maps (scale bar: 50 nm), (f) line-scan, (g) normalized atomic compositional profile, and (h) powder XRD of PtPdRhRuCu MMNs. (h) PtPdRhRuCu MMNs are compared to FCC Pt. Reproduced under terms of the CC-BY license.[75] Copyright (2023), Y. Kang, O. Cretu, J. Kikkawa, K. Kimoto, H. Nara, A. S. Nugraha, H. Kawamoto, M. Eguchi, T. Liao, Z. Sun, T. Asahi, Y. Yamauchi, published by Springer Nature.

Hydrothermal

Hydrothermal synthesis, akin to solvothermal methods, utilizes water as the primary solvent instead of organic solvents. While the methodology shares many similarities, the maximum achievable temperatures are limited to below 100 °C under standard atmospheric conditions. This limitation, coupled with challenges like NP agglomeration and stability, necessitates the use of stabilizing agents, capping agents, or support materials to ensure the stability of the synthesized nanoparticles. Additionally, pressurized reaction vessels may be required, depending on the specific approach.

A notable application of hydrothermal synthesis was demonstrated by Kang *et al.*,[75] who developed mesoporous PtPdRhRuCu HEA nanospheres for HER catalysis. The synthesis employed self-assembled micelles of the diblock copolymer PEO-*b*-PMMA, which served as a structural framework for HEA nanoparticle formation (Fig. 13a). The resulting nanospheres had an average size of approximately 128 nm (Fig. 13), with uniform mesopores of around 23 nm in diameter (Fig. 14c). Local variations in the elemental mixing were observed around the pores (Fig. 14a and c). The choice of surfactant and reducing agent significantly influenced the final morphology of the nanoparticles. For example, the surfactants F127 and PVP were compared, with F127 producing reduced mesoporosity and PVP leading to irregular nanostructures. Similarly, the reducing agent played a crucial role: strong reducing agents like dimethylamine borane caused significant nanoparticle agglomeration, while (milder) formic acid resulted in irregular pore structures.

Temperature variations also affected the synthesis outcomes, particularly influencing the Ru content in the nanoparticles. The chain length of the block copolymer PEO-*b*-PMMA was another critical factor, specifically the PMMA chain, which acted as a sacrificial template to form the mesopores. When the PEO chain length was held constant, varying the PMMA chain length showed a clear correlation with pore size in the resulting mesoporous structures. For example, PEO$_{10000}$-*b*-PMMA$_{5500}$ produced the smallest pore sizes, around 8 nm, while PEO$_{10500}$-*b*-PMMA$_{22000}$ resulted in significantly larger pores, measuring up to 41 nm. After extensive

Fig. 14 (a) PtPdRhRuCu MMN edge pore HAADF−STEM image and Energy-Dispersive X-ray Spectroscopy (EDS) maps (scale bar: 10 nm). (b) ΔS_{mix} value at the selected area found in (a) (1−4). (c) Elemental distribution of mesopore in PtPdRhRuCu MMN. Reproduced under terms of the CC-BY license.[75] Copyright (2023), Y. Kang, O. Cretu, J. Kikkawa, K. Kimoto, H. Nara, A. S. Nugraha, H. Kawamoto, M. Eguchi, T. Liao, Z. Sun, T. Asahi, Y. Yamauchi, published by Springer Nature.
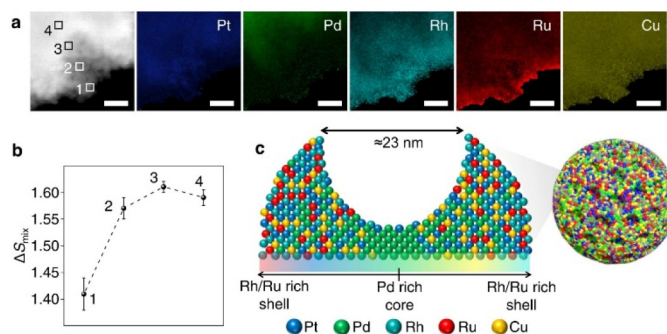
testing, PEO$_{10500}$-b-PMMA$_{18000}$, which formed pores approximately 23 nm in size, delivered the best performance for HER under alkaline conditions (1 M KOH). This composition achieved impressively low overpotentials of 10 mV to reach a current density of 10 mA cm^{-2} and exhibited a Tafel slope of 87 mV dec^{-1}. Stability tests revealed that PtPdRhRuCu nanospheres maintained stable operation for 140 hours across varying current densities from 10 to 100 mA cm^{-2}.

The challenges associated with hydrothermal synthesis are comparable to those of solvothermal methods, but certain issues are more pronounced. In particular, nanoparticle agglomeration is more significant when water is used as the solvent, necessitating the use of stabilizing or capping agents to maintain particle dispersion and stability. Additionally, the milder reaction conditions characteristic of hydrothermal synthesis amplify the influence of both the reducing agents and the stabilizing agents on the final morphology and properties of the nanoparticles. These factors must be carefully optimized to achieve the desired catalytic performance and structural stability.

Performance summary of varying high entropy alloy catalysts and synthesis methods

The tables below provide a performance summary of various reported HEA catalysts along with their respective synthesis methods. They are organized based on specific electrochemical reactions as follows: HER (Table 1), OER (Table 2), ORR (Table 3), CO$_2$ reduction (includes reaction product) (Table 4), and ammonia synthesis (Table 5). These tables illustrate the wide-ranging interests for HEA applications towards electrochemical synthesis.

Nanoscale HEA formation behavior

Despite the promising properties and potential applications of nanoscale HEAs in catalysis, a comprehensive understanding of their formation mechanisms is still lacking. In this concluding section, we aim to summarize current findings and provide insights into the fundamental processes underlying HEA formation. We will explore specific formation mechanisms observed at the nanoscale, with a particular emphasis on experimental studies conducted through wet synthesis techniques. The milder reaction conditions characteristic of wet synthesis methods enable the analysis of products at sequential stages of the synthesis process. This provides unique opportunities to gain deeper insights into the conditions and pathways through which HEAs form, allowing researchers to capture key intermediate states and mechanisms that drive their formation.

High entropy alloy formation mechanisms in wet chemistry methods

Wet-chemistry (hydrothermal/solvothermal) synthesis of HEAs typically involves two distinct phases: an initial reduction phase under heating, which may directly yield HEAs, and an additional annealing step often required to achieve a homogeneous HEA phase. The annealing phase is typically validated by characterization techniques such as XRD to assess phase uniformity and elemental mapping using XPS, EDS, or Electron Energy Loss Spectroscopy (EELS) to confirm HEA formation.

Despite its importance, the role of temperature during the initial reduction phase remains underexplored. Reported initial reduction temperatures range from room temperature to as high as 280 °C. Similarly, annealing times and temperatures exhibit significant variation. While some methods bypass the need for annealing, others require temperatures ranging from 350 °C to 700 °C for durations exceeding two hours. Notably, HEA-NPs have been successfully synthesized under remarkably mild conditions, such as reduction at room temperature and without annealing. Even when annealing is utilized, the required temperatures are substantially lower than the melting points of the precursor metals. In contrast, bulk-phase HEA synthesis typically demands the complete melting of all precursor metals.

These mild reaction conditions suggest the involvement of additional mechanisms that are not yet fully understood and are less prominent at the bulk scale. Factors such as atomic diffusion and reducing agent interactions require closer examination, as atomic diffusion is significantly accelerated at elevated temperatures and becomes more pronounced at the nanoscale. Additionally, the complex interactions and kinetics between reducing agents and precursor materials can influence mixing and composition at various stages of the synthesis process. A deeper understanding of these factors could be crucial in determining the temperatures required for nanoscale HEA formation and may challenge the current explanation of entropy-driven material formation.

For example, a study by Chen et al.[74] demonstrated the synthesis of convex cube-shaped Pt$_{34}$Fe$_5$Ni$_{20}$Cu$_{31}$Mo$_9$Ru HEA nanocrystals via a solvothermal method under mild conditions (220 °C for 2 hours). Demonstrating the feasibility of the synthesis as well as demonstrating outstanding electrocatalytic performance. The study demonstrated unique nanocrystal morphologies compared to many other HEA synthesis methods, with two specific shapes observed: cube-shaped structures after one hour of heating and converged cube-shaped structures after two hours. These time-dependent studies provide valuable insights into the mechanism at the nanoscale. More detailed investigations in future studies, including intermediate characterization and exploration of temperature and time effects, would help clarify the mechanisms underlying HEA formation at the nanoscale. This deeper understanding could also aid in developing new synthesis strategies and addressing challenges such as preventing intermetallic formation and phase separation.

Seed-mediated HEA formation pathway

The seed-mediated formation process for HEAs has been reported in hydrothermal and solvothermal synthesis

Table 1 Hydrogen evolution reaction performance of various reported HEA catalysts

Composition	Electrolyte	Overpotential at 10mA cm^{-2}	Tafel slope (mV dec^{-1})	Synthesis method	Stability	Ref.
TiNbTaCrMo	Seawater	960 mV at 50 mA cm^{-2}	96.33	Arc-discharge	Stable for 10 hours at 863 mV overpotential	80
Ni$_{20}$Fe$_{20}$Mo$_{10}$Co$_{35}$Cr$_{15}$	1 M KOH	172 mV	66	Arc-melting	Stable for 8 hours at 100 mA cm^{-2} 0.5 M H$_2$SO$_4$	71
RhRuPtPdIr	0.5 M H$_2$SO$_4$	58 mV	42	Atomic layer deposition	7.5% current density decrease after 20 hours	81
FeCoNiMnCr	1 M KOH	190 mV	64	Single-step pyrolysis	15% current density decrease after 6 hours	30
FeCoNiCuMn	1 M KOH	115 mV	94.2	CTS	Stable for 50 hours at 50 mA cm^{-2}	82
PtNiCoFeCu	1 M KOH	7 mV	58	CTS	Stable for 500 h maintaining 100 mA cm^{-2}	83
PtIrFeNiCoCe	0.1 M KOH	193 mV	91.1	CTS	Stable for over 5000 cycles	84
AlNiCoIrMo	0.5 M H$_2$SO$_4$	275 mV	33.2	De-alloying	Stable for 48 hours at 1.52 V^a	29
AlAgAuCoCuFeIrNiPdPtRhRuMoTi	0.5 M H$_2$SO$_4$	32 mV	30.1	De-alloying	Stable for 10 hours at 10 mA cm^{-2}	85
AlAgAuCoCuFeIrNiPdPtRhRu	0.5 M H$_2$SO$_4$	42 mV	38.3	De-alloying	N/A	85
AlNiCoRuMo	1 M KOH	24.5 mV	30.3	De-alloying	N/A	86
PtPdRhIrNi	1 M KOH	55 mV	44.8	De-alloying	21 mV increase after 24 hours	87
ZnNiCoIrMn	0.1 M HClO$_4$	50 mV at 50 mA cm^{-2}	30.6	De-alloying	16.8 mV increase after 100 hours at 10 mA cm^{-2}	88
CuCrFeNiCoP	1 M KOH	365 mV at 100 mA cm^{-2}	118	Electrodeposition	Stable for 48 hours at 100 mA cm$^{-2\,a}$	89
FeCoNiCuMn	1 M KOH	281 mV at 100 mA cm^{-2}	53	Electrospun nanofiber	Stable over 20 hours at 170 mA cm^{-2}	90
PtCoCuFeMnNi	0.5 M H$_2$SO$_4$	70 mV	47	Electrodeposition	Stable for 27 hours at 10 mA cm^{-2}	91
CoFeLaNiPt	0.1 M KOH	555 mV	N/A	Electrodeposition	Stable for 10 hours at 377 mV overpotential	92
FeCoPdIrPt	1 M KOH	42 mV	82	Fast-moving bed pyrolysis	Stable for 150 hours at 10 mA cm^{-2}	79
PtZrNbFeCuTaMoHfBiWZnSnPdNi	1 M KOH	18 mV	30.7	Hydrothermal	3 mV decrease after 264 hours at 100 mA cm^{-2}	93
NiCoFePtRh	0.5 M H$_2$SO$_4$	27 mV	30.1	Hydrothermal	8.4% decrease in current density after 100 hours	31
FeCoNiCuIr	0.1 M HClO$_4$	71 mV	41.7	Hydrothermal	2 mV overpotential increase after 48 hours 100 mA cm^{-2}	32
PtPdRhRuCu	1 M KOH	10 mV	87	Hydrothermal	Stable for 140 hours running at varying current densities from 10 to 100 mA cm^{-2}	75
FeCoNiCuPtIr	1 M KOH	21 mV	54.5	Laser	Negligible increase after 24 hours at 10 mA cm$^{-2\,a}$	94
FeCoNiCrN	1 M KOH	161.8 mV	124.5	Laser	Stable for 10 hours at 100 mA cm$^{-2\,a}$	95
PtIrCuNiCr	1 M KOH	300 mV^a	N/A	Laser/solvothermal	Stable for 72 hours at 200 mA cm$^{-2\,a}$	96
CuNiFeCoCrTi	1 M KOH	117.11 mV	95.32	Mechanical alloying	Stable for 500 hours at 10 mA cm^{-2}	97
FeCoNiCuPd	1 M KOH	29 mV	47.2	Magnetron sputtering	Stable for 24 hours at 100 mA cm$^{-2\,a}$	98
CoCrFeNiAl	0.5 M H$_2$SO$_4$	73 mV	39.7	Mechanical alloying	Stable for 12 hours at 10 mA cm^{-2}	99
IrPdPtRhRu	1 M KOH	60 mV	42	Plasma reduction	Stable for 6 hours at 100 mA cm^{-2}	100
FeNiCoMnVO$_x$	1 M KOH	89 mV	88	Plasma regulated synthesis	Stable for 100 hours at 10 mA cm^{-2}	101
NiCoFeMnCrP	1 M KOH	220 mV	94.5	Sol–gel	Stable for 24 hours at 1.55 V^a	102
Pt$_{34}$Fe$_5$Ni$_{20}$Cu$_{31}$Mo$_9$Ru	1 M KOH	20 mV	27	Solvothermal	5% decrease in current density after 40 hours	74
IrPdPtRhRu	1 M HClO$_4$	6 mV	N/A	Solvothermal	50% decrease in current density after 6 hours	103
PdPtRhIrCu	1 M KOH	15 mV	37	Solvothermal	Stable for 20 hours at 10 mA cm^{-2}	34
Pt$_{18}$Ni$_{26}$Fe$_{15}$Co$_{14}$Cu$_{27}$	1 M KOH	11 mV	30	Solvothermal	Stable for 10 hours maintaining 10 mA cm^{-2}	35
Pt$_{28}$Mo$_6$Pd$_{28}$Rh$_{27}$Ni$_{15}$	1 M KOH	9.7 mV	25.9	Solvothermal	6.9 mV increase after 30 hours 10 mA cm^{-2}	104
IrPdRhMoW	0.5 M H$_2$SO$_4$	15 mV	35	Solvothermal	Stable for 100 hours at 100 mA cm$^{-2\,a}$	36
PdFeCoNiCu	1 M KOH	18 mV	39	Solvothermal	Negligible increase after 15 days at 10 mA cm^{-2}	37
PdMoGaInNi	0.5 M H$_2$SO$_4$	13 mV	179.8	Solvothermal	No increase after 12 hours at 10 mA cm^{-2}	38
PtAuPdRhRu	1 M KOH	190 mV at 30 mA cm^{-2}	62	Ultrasonic	Stable for 8 hours at 100 mA cm^{-2}	78

^{a} Overall water splitting.

methods. This process begins with initial reduction leading to the formation of an NP seed that is rich in one or two elements. The initial NP seed assists in the further reduction of precursor elements by acting as the preferential site for their deposition and growth. The remaining elements can either mix homogenously or form a core–shell structure. The system undergoes additional heating to achieve homogeneous HEA nanoparticles, either by increasing the reaction tempera-

Table 2 Oxygen evolution reaction performance of various reported HEA catalysts

Composition	Electrolyte	Overpotential at 10 mA cm^{-2}	Tafel slope (mV dec^{-1})	Synthesis method	Stability	Ref.
FeCoNiCuCr	1 M KOH	330 mV	94	Ball milling	Stable for 25 000 seconds, maintaining 25 mA cm^{-2}	105
FeCoNiMnCr	1 M KOH	350 mV	95	Single-step pyrolysis	15% decrease in current density after 6 hours	30
(MgFeCoNiZn)O	1 M KOH	350 mV at 100 mA cm^{-2}	44.9	CTS	Stable for 20 000 seconds	106
PtIrFeNiCoCe	0.1 M KOH	485 mV	119.1	CTS	Stable for 5000 cycles	84
AlNiCoIrMo	0.5 M H$_2$SO$_4$	255 mV at 20 mA cm^{-2}	55.2	De-alloying	11.5 mV increase after 7000 cycles	29
AlNiCoIrMo	0.5 M H$_2$SO$_4$	275 mV ^{a}	55.2	De-alloying	Stable for 48 hours at 1.52 V ^{a}	29
AlAgAuCoCuFeIrNiPdPtRhRuMoTi	0.5 M H$_2$SO$_4$	274 mV	121.1	De-alloying	N/A	85
AlAgAuCoCuFeIrNiPdPtRhRu	0.5 M H$_2$SO$_4$	258 mV	84.2	De-alloying	Stable for 40 000 seconds at 10 mA cm^{-2}	85
MnNiCuCoVFeMoPdPtAuRuIr	1 M KOH	263 mV	82.5	De-alloying	Stable for 100 hours at 1.49 V	107
AlNiCoRuMo	1 M KOH	150 mV	54.5	De-alloying	—	86
AlNiCoFeMo	1 M KOH	240 mV	46	De-alloying	Stable for 2000 cycles	108
ZnNiCoIrMn	0.1 M HClO$_4$	237 mV	46	De-alloying	Maintaining 1.52 V vs. RHE for 100 hours at 10 mA cm^{-2}	88
CuCrFeNiCoP	1 M KOH	423 mV at 100 mA cm^{-2}	70.7	Electrodeposition	Stable for 48 hours at 100 mA cm^{-2} ^{a}	89
FeCoNiCuMn	1 M KOH	386 mV at 200 mA cm^{-2}	69	Electrospun nanofiber	Stable for 20 hours at 230 mA cm^{-2}	90
CoFeLaNiPt	0.1 M KOH	377 mV	N/A	Electrodeposition	Stable for 10 hours at 557 mV overpotential	92
FeCoNiIrRu	0.5 M H$_2$SO$_4$	241 mV	153	Electrospinning method	Stable for 14 hours at 10 mA cm^{-2}	109
NiCoNiZnV	1 M KOH	274 mV	59	Hydrothermal	Stable for 100 hours at 1.5 V vs. RHE	110
MgMnFeCoNi	1 M KOH	354 mV at 100 mA cm^{-2}	46.8	Hydrothermal	Stable for 10 hours at 10 mA cm^{-2}	33
FeCoNiCuPtIr	1 M KOH	255 mV	61.7	Laser	Negligible increase after 24 hours at 10 mA cm^{-2} ^{a}	94
FeCoNiCrN	1 M KOH	269.7 mV	42.5	Laser	Minimal overpotential increase after 50 000 seconds at 10 mA cm^{-2}	95
PtIrCuNiCr	1 M KOH	300 mV ^{a}	N/A	Laser/solvothermal	Stable for 72 hours at 200 mA cm^{-2}	96
FeCoNiCuPd	1 M KOH	194 mV	39.8	Magnetron sputtering	Stable for 36 hours at 100 mA cm^{-2}	98
IrFeCoNiCu	0.1 M HClO$_4$	302 mV	58	Microwave-assisted shock	Less than 60 mV increase in overpotential after 12 hours at 10 mA cm^{-2}	28
NiCoFeMnCrP	1 M KOH	270 mV	52.5	Sol–gel	Stable for 24 hours at 1.55 V vs. RHE	102
Pt$_{34}$Fe$_5$Ni$_{20}$Cu$_{31}$Mo$_9$Ru	1 M KOH	259 mV	39	Solvothermal	8% reduction in current density after 40 hours	74
IrPdRhMoW	0.5 M H$_2$SO$_4$	188 mV	60	Solvothermal	stable for 100 hours at 100 mA cm^{-2} ^{a}	36
MnFeCoNiCu	1 M KOH	263 mV	43	Solvothermal	Stable for 24 hours maintaining a current density of 10 mA cm^{-2}	111
AlCrCuFeNi	1 M KOH	250 mV	77.5	De-alloying	Stable for 35 hours at 290 mV overpotential	112

^{a} Overall water splitting.

ture, extending the heating duration, or by annealing the catalyst material in a high-temperature furnace.

When using a seed-mediated approach for HEA synthesis, several key factors must be carefully considered. First, the seed particles must be monodispersed to enhance shell uniformity. Second, the choice of supporting ligands or capping agents is crucial, as they influence shell deposition. Lastly, the final HEA stoichiometry is determined by the relative sizes of the seed and shell. Kar et al.,[123] synthesized various HEA systems using a combination of seed-mediated synthesis and thermal annealing. By systematically varying the seed and shell compositions, they explored different metal combinations, including Pd, Cu, Pt, Ni, Co, Au, Ag, and Sn. Their study provided a comprehensive analysis of how the interplay between seed and

Table 3 Oxygen reduction reaction performance of various reported HEA catalysts

Composition	Electrolyte	Half-wave potential	Mass activity A mg⁻¹ noble metal	Synthesis method	Stability	Ref.
$Pt_{34}Fe_5Ni_{20}Cu_{31}Mo_9Ru$	0.1 M HClO₄	0.87 V	11.4 A mg⁻¹ Pt	Solvothermal	11% current density reduction after 40 hours	74
PtZrNbFeCuTaMoHfBiWZnSnPdNi	0.1 M KOH	0.86 V	N/A	Solvothermal	4.8% current density reduction after 120 hours	93
AlNiCoRuMo	1 M KOH	0.875 V	N/A	De alloying	Stable for 20 000 cycles	86
AlCuNiPtMn	0.1 M KOH	0.954 V	N/A	De alloying	9.1% current density reduction after 164 hours	113
AlCuNiPtMn	0.1 M HClO₄	0.945 V	0.3466 A mg⁻¹ Pt	De alloying	N/A	113
PtPdFeCoNi	1 M KOH	0.85 V	N/A	CTS	29% current density reduction after 15 hours	114
HfZrLaVCeTiNdGdYPd	0.1 M KOH	0.85 V	0.49 A mg⁻¹ Pd	CTS	14% current density reduction after 100 hours	115
PdCuPtNiCo	0.1 M KOH	0.83 V	0.176.1 A mg⁻¹ Pt	Furnace pyrolysis	5 mV increase half-wave potential after 10 000 cycles	116
PtPdRhFeCoNi	0.1 M KOH	0.85 V	N/A	Laser	half wave increased after 5000 cycles	117
CoFeNiCuPd	0.1 M KOH	0.9 V	2.037 A mg⁻¹ Pd	Annealed on mesoporous material	10 mV decrease half-wave potential after 10 000 cycles	118

Table 4 CO₂ reduction reaction performance of various reported HEA catalysts

Composition	Solution	Onset potential	Reaction	Mass activity A mg⁻¹ noble metal	Synthesis method	Stability	Ref.
PtZrNbFeCuTaMoHfBiWZnSnPdNi	1 M KOH + 1 M CH₃OH	395 mV	MOR	12.6 A mg⁻¹$_{Pt}$	Solvothermal	28.7% decrease in current density after 10 000 seconds	93
$Pt_{18}Ni_{26}Fe_{15}Co_{14}Cu_{27}$	1 M KOH + 1 M CH₃OH	391 mV	MOR	10.96 A mg⁻¹$_{Pt}$	Solvothermal	Stable for 5000 seconds at 0.65 vs. RHE	35
PtRhBiSnSb	1 M KOH + 1 M C₂H₅OH	N/A	EOR	15.558 A mg⁻¹$_{Pt+Rh}$	Solvothermal	Stable for 20 000 seconds at 0.65 vs. RHE	119
PtRhBiSnSb	1 M KOH + 1 M CH₃OH	N/A	MOR	19.529 A mg⁻¹$_{Pt+Rh}$	Solvothermal	Stable for 20 000 seconds at 0.7 vs. RHE	119
NiCoFePB	1 M KOH + 1 M CH₃OH	1.27 V	MOR	15.04 A mg⁻¹$_{Pt}$	Sol–gel synthesis	5% decrease in current density after 3600 seconds	120
PdPtCuPbBi	1 M KOH + 1 M C₂H₅OH	300 mV	EOR	18.21 A mg⁻¹$_{Pd+Pt}$	Template-assisted method	maintained 2.56 A mg⁻¹$_{Pd+Pt}$ for 20 000 seconds	121

Table 5 Ammonia synthesis reaction performance of various reported HEA catalysts

Composition	Electrolyte	Faradaic efficiency	Yield	Synthesis method	Stability	Ref.
NiCoNiZnV	0.05 M H₂SO₄ + 1 M KOH	14.75% at −1.45 V vs. RHE	42.76 µg hmg$_{cat}$⁻¹ at −1.45 V vs. RHE	Hydrothermal synthesis	N/A	110
$(Co_{0.2}Ni_{0.2}Zn_{0.2}Mg_{0.2}Cu_{0.2})Fe_2O_4$	0.1 M KNO₃ + 1 M KOH	98.1% at −0.5 V vs. RHE	2.1 mmol hcm⁻² at −0.5 V vs. RHE	Sol–gel synthesis	Stable for 50 cycles	122

shell compositions influences core–shell formation, ultimately shaping the final HEA composition.

The study begins by investigating the role of metals with different redox potentials in core–shell formation. Using monodispersed PdCu, PdAg, PdCo, and PdAu seeds, the researchers examined how galvanic replacement influences shell growth when Pd is paired with metals of varying reduction potentials. Through TEM (Fig. 15a, b and f, g), STEM-EDS elemental mapping (Fig. 15c and h), and linescan analysis (Fig. 15d and i), they determined that for a core–shell
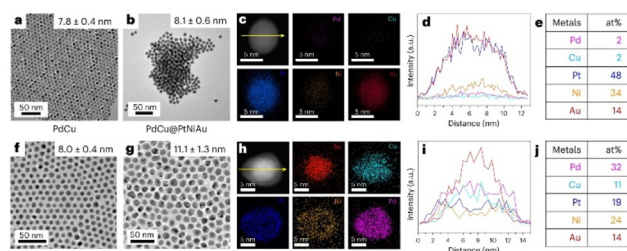
Fig. 15 TEM images of PdCu seed (a) and PdCu seeds with PtNiAu shell (b). EDS Map (c), linescan (d), and atomic% break down (e) of PdCu@PtNiAu core shell NPs (b). TEM images of AuCu seed (f) and AuCu seeds with PdPtNi shell (g). EDS Map (h), linescan (i), and atomic% break down (j) of AuCu@PdPtNi core shell NPs (g). Adapted from ref. 123 Copyright (2023), with permission from Springer Nature.

structure to form, the core metals must have a higher redox potential than the shell metals. When synthesizing PdPtCuNiAu HEAs using either monodispersed PdCu or AuCu seeds, they observed that Au, having a higher reduction potential than both Pd and Cu, significantly influenced elemental distributions due to galvanic replacement. Specifically, when PdCu was used as the seed and Au was in the shell, both Pd and Cu exhibited depletion in elemental maps and linescan data (Fig. 15c–e).

Conversely, in PdCoPtNiCu systems with PdCo seeds (Fig. 16a–e), only Co was depleted (Fig. 16e), as it had the lowest redox potential among the core metals. Lattice mismatch effects were further investigated using PdSnPtNiCu HEA systems. Sn favors a BCC structure, whereas the remaining constituent elements predominantly adopt an FCC structure, resulting in inherent lattice mismatch. Consequently, when Sn was used to form the shell on PdCu seeds, it exhibited both homogeneous nucleation and heterogeneous nucleation, and growth, on the PdCu seeds (Fig. 16g). Therefore, metals that tend to hinder alloy phase formation or have poor wettability should go in the seed of the core–shell NPs. The study emphasizes the critical importance of accounting for redox potential and lattice mismatch when designing HEAs, as these factors directly influence the structural and compositional outcomes
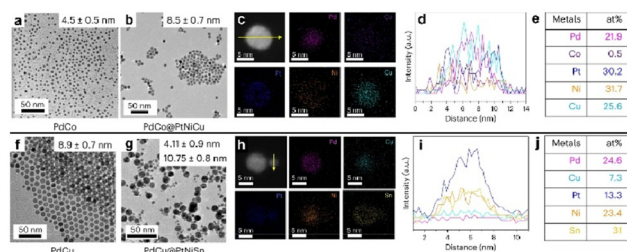
of seed-mediated HEA synthesis. Furthermore, the findings encourage further investigation, as the observed effects are closely related to key empirical parameters governing HEA formation. Further research could focus on exploring VEC and electronegativity effects on HEA NP formation.

Co-reduction HEA formation pathway

Though direct investigation of HEA NP formation is limited, two primary mechanisms are commonly cited for the formation of HEA NPs through wet chemistry methods. These being the co-reduction mechanism and the seed-mediated mechanism.[31,36,93,123–125]

The co-reduction mechanism refers to the simultaneous reduction of all the elements in an HEA precursor mixture, facilitating their homogeneous mixing and the subsequent formation of HEA NPs. Co-reduction as a proposed mechanism is particularly interesting as an additional annealing step is not mandatory in some reported cases. However, even in co-reduction processes, annealing may still be employed to enhance phase uniformity, such as achieving a well-defined FCC or BCC phase single-phase HEA.

Sun et al.,[124] investigated the co-reduction of Au, Ag, Pt, Cu, and Pd metal salts using poly(ethylene glycol) methyl ether thiol (mPEG–SH) ligands and being reduced by sodium borohydride (NaBH$_4$). The resulting single and polycrystalline nanoparticles ranged in diameters from 0.5 nm to 3 nm. HAADF-STEM images revealed the coexistence of sub-nanometer, non-crystalline metal clusters alongside the synthesized nanoparticles (Fig. 18f). The authors subsequently varied the metal-to-ligand ratios used during synthesis to further investigate the HEA formation (Fig. 17a–c). It was observed that a high metal-to-ligand ratio (5 : 1) resulted in the formation of phase-separated core–shell nanoparticles (Fig. 17c and f). The authors highlight that thiol ligands react with metal ions to form metal thiolates, which exhibit similar reduction rates across all metals thiolates. However, if insufficient thiol ligands are present, the remaining metal ions will have varying reduction rates.

However, a 1 : 1 metal-to-ligand ratio was identified as optimal due to the smaller particle size and improved size distribution compared to higher ratios. However, the resulting
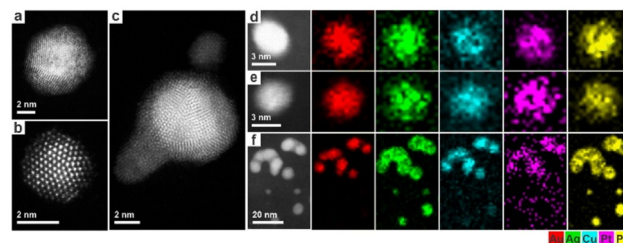

Fig. 16 TEM images of PdCo seed (a) and PdCo seeds with PtNiCu shell (b). EDS Map (c), linescan (d), and atomic% break down (e) of PdCo@PtNiCu core shell NPs (b). TEM images of PdCu seed (f) and PdCu seeds with PtNiSn shell (g). EDS Map (h), linescan (i), and atomic% break down (j) of PdCu@PtNiSn core shell NPs (g). Adapted from ref. 108 and 123 Copyright (2023), with permission from Springer Nature.

Fig. 17 AuAgCuPtPd HEA NPs synthesized with different metal : ligand ratios: (a and d) 1 : 1, (b and e) 2.5 : 1, and (c and f) 5 : 1. (a–c) HAADF-STEM images of HEA NPs, with corresponding EDS elemental maps shown in (d–f). Reproduced from ref. 124 Copyright (2023), with permission from RSC publishing.

parameter changes still did not fully explain the presence of sub-nano clusters. Subsequently, liquid phase TEM (LPTEM) using aqueous medium and reduction by electron beam was used to study the HEA NP formation. The use of aqueous medium with electron beam reduction had similar reaction kinetics to that of $NaBH_4$ when using mPEG-SH ligands. Given the spatial resolution limitations of the experimental setup, metal-to-ligand ratios of 1 : 1.5 and 1 : 2 were selected to produce larger nanoparticles, ensuring clearer imaging and more accurate analysis (Fig. 18a and b). Using LPTEM, nanoparticle growth was tracked in real-time, revealing the formation of large aggregates (10–20 nanoparticles per cluster) (Fig. 18a–c). Interestingly, despite this aggregation, the nanoparticles exhibited independent, isotropic growth, maintaining clear interparticle separation before reaching their final size of 5–10 nm within 30–60 seconds.

Further HAADF-STEM images of the samples after electron beam reduction detected sub-nanometer metal clusters (Fig. 18f), suggesting that HEA formation deviates from classical nucleation theory and Lamer's model. In a follow-up experiment to investigate the role of supersaturation, the researchers returned to the original synthesis method using $NaBH_4$ as the reducing agent and analyzed its effect on HEA formation by varying its concentration. The results showed that higher $NaBH_4$ levels led to increased nanoparticle size

and aggregation, supporting previous reports that $NaBH_4$ can displace ligands.

Based on these findings, the authors proposed a non-classical nucleation mechanism for HEA formation. In their model, $NaBH_4$ rapidly reduces all metal salts, generating small, ligand-stabilized metal clusters. Subsequently, borohydride and hydride ions displace the ligands, triggering cluster aggregation and ultimately forming HEA (Scheme 4). The study highlights the complex interactions between supporting ligands and reducing agents and their impact on HEA formation. Further research on the complexity of HEA formation mechanisms will help in developing a comprehensive understanding of the synthesis process.

Recent comprehensive investigations into the formation mechanisms of HEA NPs by Dey et al.,[125] utilized a solvothermal synthesis approach to explore the time evolution of HEA formation across seven distinct systems. Through detailed investigations, the study revealed that different systems follow unique formation pathways depending on their elemental composition. The study initially focused on noble metals Pd, Pt, Rh, and Ir combined with other transition metals and a post-transition metal, Sn. For the NiPdPtRhIr system, the synthesis began with the formation of Pd-rich seeds that served as templates for the gradual incorporation of other metals, ultimately achieving equimolar compositions (Fig. 19). This seed-mediated mechanism was analyzed by collecting and evaluating samples at various time intervals using TEM and EDS. Subsequent composition changes with further transition metal additions resulted in the same seed-mediated formation pathway for NiFeCoPdPt, NiFePdPtIr, and NiFeCoPdPtIr systems.
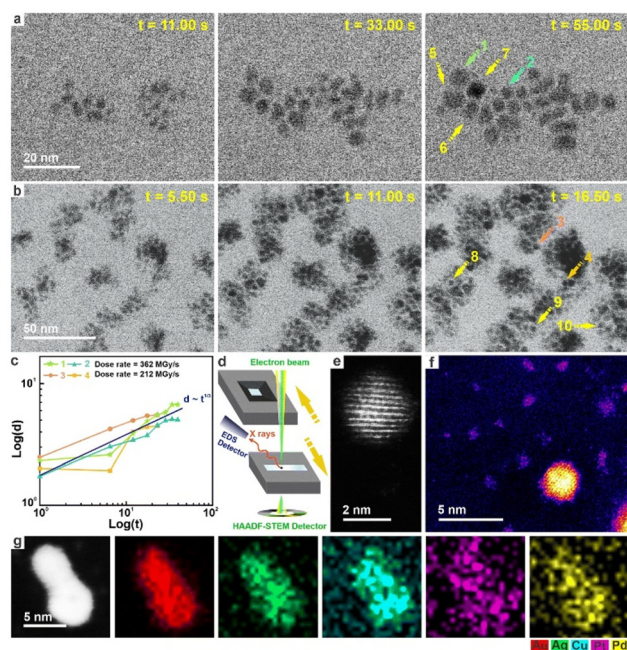

Fig. 18 Time-lapsed LPTEM of AuAgCuPtPd HEA NP formation with metal : ligand ratios of (a) 1 : 1.5 and (b) 1 : 2. (c) Plot of particle growth over time tracking particles (1–4) from (a and b). (d) Schematic of characterization setup of dried liquid cell window. (e) HAADF-STEM image HEA NPs after LPTEM synthesis. (f) Sub-nanometer clusters found in HAADF-STEM image of AuAgCuPtPd HEA NPS after LPTEM synthesis. (g) HAADF-STEM image and EDS maps of LPTEM synthesized AuAgCuPtPd HEA NP. Reproduced from ref. 124 Copyright (2023), with permission from RSC publishing.
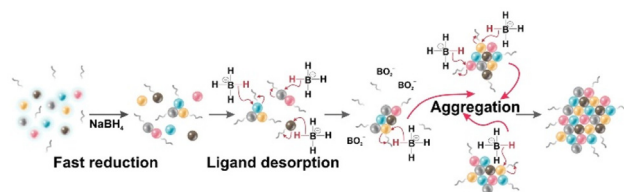
Scheme 4 Schematic of HEA formation due to $NaBH_4$ and ligand interactions. Reproduced from ref. 124 Copyright (2023), with permission from RSC publishing.
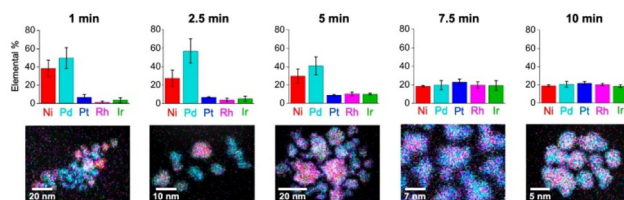

Fig. 19 EDS maps of NiPdPtRhIr HEA NP formation at various time intervals (1, 2.5, 5, 7.5, and 10 minutes), accompanied by bar charts illustrating the corresponding elemental composition changes. Reproduced from ref. 125 Copyright (2023), with permission from American chemical society.

The most intriguing findings emerged when noble metals were combined with the p-block element Sn. In the SnPdPtRhIr system, the metals underwent simultaneous co-reduction and mixing, deviating from the seed-mediated growth observed in other systems. However, the order of precursor addition was crucial. If the Sn precursor was injected first, followed by the remaining metal precursors then PdSn rich nanoparticles were formed initially (seed mediated growth). In contrast, injecting Sn after the other precursors led to co-reduction. Interestingly, Sn alone did not induce a color change in the reaction flask, indicating that the chosen reducing agent could not reduce Sn salts in the absence of other metal precursors. Therefore, it is crucial to study the interaction between reducing agents and individual metal precursors. As it not only reveals possible redox interactions between precursor metals but also highlights potential causes of proportional discrepancies, even when equiatomic ratios are used.

The role of Sn in HEA formation was also further investigated in the study using a NiSnPdPtIr system. Interestingly characteristics of both pathways were observed for this system.

Overall, these studies underscore the significant influence of elemental composition on the formation pathways of HEA NPs. The distinct mechanisms of seed-mediated growth, co-reduction, and hybrid pathways, highlight the complexity of HEA NPs synthesis. In particular, the role of elements such as Sn in modulating reduction dynamics suggests new opportunities for tailoring HEA structures through strategic precursor selection.

Summary and outlook

As the world transitions toward renewable energy sources and the sustainable production of high-value chemicals, the demand for cost-effective, high-performance catalysts has become increasingly urgent. HEAs have demonstrated superior catalytic performance compared to conventional platinum group metal-based catalysts, while also offering significantly enhanced stability. However, despite their promising potential, the study of HEAs remains in its early stages.

This review discussed the synthesis of HEAs under mild conditions, which presents several advantages over more conventional top-down methods. Notably, many of the discussed synthesis techniques facilitate the study and characterization of reaction intermediates as well as catalyst–support interactions. One of the most intriguing aspects of these mild synthesis conditions is the significantly lower temperatures required compared to their top-down counterparts. Both seed-mediated and co-reduction formation pathways demonstrate substantially reduced temperatures, challenging the prevailing notion that HEAs can only form under high-temperature conditions.

Overall, the outlook for HEAs in electrocatalysis appears promising. Given the relatively early stage of the field, many fundamental questions regarding material properties, formation mechanisms, and catalytic performance remain unan-swered. We emphasize the need for more rigorous research in several key areas of nanoscale HEA synthesis.

First, further investigation into reduction methods is crucial, as few studies have systematically examined the impact of reduction rates independent of temperature or ligand interactions. Second, a deeper understanding of initial reduction conditions is needed to explore their potential for substituting or modifying annealing requirements. Faster diffusion rates and enhanced atomic mobility during reduction could lower the temperatures and durations required for final annealing, improving overall efficiency. Finally, continued research into the catalytic properties of HEAs will be essential for guiding the design of next-generation catalysts and accelerating the development of low-cost, noble-metal-free alternatives.

The commercialization of nanoscale HEAs will ultimately depend on the development of scalable, cost-effective synthesis methods with reduced energy demands. Advancing these aspects will be key to unlocking their full potential for sustainable catalysis applications.

Author contributions

V. Maheshwari: funding acquisition, resources, supervision – review & editing. A. Li: conceptualization, data curation, investigation, writing – original draft. N. Qureshi: data curation, investigation, visualization, writing – original draft.

Conflicts of interest

There are no conflicts to declare.

Data availability

No primary research results, software or code have been included and no new data were generated or analysed as part of this review.

Acknowledgements

References

1 Executive Summary – CO2 Emissions in 2023 – Analysis, https://www.iea.org/reports/co2-emissions-in-2023/executive-summary, (accessed December 2, 2024).

2 M. I. Khan and S. G. Al-Ghamdi, *Int. J. Hydrogen Energy*, 2023, **48**, 10315–10344.

3 A. Ajanovic, M. Sayer and R. Haas, *Int. J. Hydrogen Energy*, 2022, **47**, 24136–24154.

4 H. Tüysüz, *Acc. Chem. Res.*, 2024, **57**, 558–567.

5 O. Schmidt, A. Gambhir, I. Staffell, A. Hawkes, J. Nelson and S. Few, *Int. J. Hydrogen Energy*, 2017, **42**, 30470–30492.

6 D. R. MacFarlane, P. V. Cherepanov, J. Choi, B. H. R. Suryanto, R. Y. Hodgetts, J. M. Bakker, F. M. Ferrero Vallana and A. N. Simonov, *Joule*, 2020, **4**, 1186–1205.

7 D. B. Miracle and O. N. Senkov, *Acta Mater.*, 2017, **122**, 448–511.

8 M.-H. Tsai and J.-W. Yeh, *Mater. Res. Lett.*, 2014, **2**, 107–123.

9 B. Cantor, *Prog. Mater. Sci.*, 2021, **120**, 100754.

10 X. Yan, Y. Zhou and S. Wang, *Adv. Funct. Mater.*, 2025, **35**(2), 2413115.

11 W. Wan, K. Liang, P. Zhu, P. He and S. Zhang, *J. Mater. Sci. Technol.*, 2024, **178**, 226–246.

12 X. Li and X. Meng, *Int. J. Hydrogen Energy*, 2024, **82**, 1471–1480.

13 X. Huo, H. Yu, B. Xing, X. Zuo and N. Zhang, *Chem. Rec.*, 2022, **22**, e202200175.

14 X. Sun and Y. Sun, *Chem. Soc. Rev.*, 2024, **53**, 4400–4433.

15 J.-W. Yeh, S.-K. Chen, S.-J. Lin, J.-Y. Gan, T.-S. Chin, T.-T. Shun, C.-H. Tsau and S.-Y. Chang, *Adv. Eng. Mater.*, 2004, **6**, 299–303.

16 B. Cantor, I. T. H. Chang, P. Knight and A. J. B. Vincent, *Mater. Sci. Eng., A*, 2004, **375–377**, 213–218.

17 F. Zhang, C. Zhang, S. L. Chen, J. Zhu, W. S. Cao and U. R. Kattner, *Calphad*, 2014, **45**, 1–10.

18 A. Li and X. Zhang, *Acta Metall. Sin.*, 2009, **22**, 219–224.

19 C.-Y. Hsu, J.-W. Yeh, S.-K. Chen and T.-T. Shun, *Metall. Mater. Trans. A*, 2004, **35**, 1465–1469.

20 A. Mehta and Y. Sohn, *ACS Comb. Sci.*, 2020, **22**, 757–767.

21 A. Mehta and Y. Sohn, *Metall. Mater. Trans. A*, 2020, **51**, 3142–3153.

22 W. Dong, Z. Zhou, M. Zhang, Y. Ma, P. Yu, P. K. Liaw and G. Li, *Metals*, 2019, **9**, 867.

23 K.-Y. Tsai, M.-H. Tsai and J.-W. Yeh, *Acta Mater.*, 2013, **61**, 4887–4897.

24 R. Wang, W. Chen, J. Zhong and L. Zhang, *J. Mater. Sci. Technol.*, 2018, **34**, 1791–1798.

25 A. Mehta and Y. Sohn, *Mater. Res. Lett.*, 2021, **9**, 239–246.

26 J. Dąbrowa, M. Zajusz, W. Kucza, G. Cieślak, K. Berent, T. Czeppe, T. Kulik and M. Danielewski, *J. Alloys Compd.*, 2019, **783**, 193–207.

27 J. Dąbrowa and M. Danielewski, *Metals*, 2020, **10**, 347.

28 A. L. Maulana, P.-C. Chen, Z. Shi, Y. Yang, C. Lizandara-Pueyo, F. Seeler, H. D. Abruña, D. Muller, K. Schierle-Arndt and P. Yang, *Nano Lett.*, 2023, **23**, 6637–6644.

29 Z. Jin, J. Lv, H. Jia, W. Liu, H. Li, Z. Chen, X. Lin, G. Xie, X. Liu, S. Sun and H.-J. Qiu, *Small*, 2019, **15**, 1904180.

30 G. Raj, R. Nandan, K. Kumar, D. B. Gorle, A. B. Mallya, S. M. Osman, J. Na, Y. Yamauchi and K. K. Nanda, *Mater. Horiz.*, 2023, **10**, 5032–5044.

31 G. Feng, F. Ning, J. Song, H. Shang, K. Zhang, Z. Ding, P. Gao, W. Chu and D. Xia, *J. Am. Chem. Soc.*, 2021, **143**, 17117–17127.

32 S. Choi, J. Kwon, C. Park, K. Park, H. B. Park, U. Paik and T. Song, *Energy Fuels*, 2023, **37**, 18128–18136.

33 H. Wu, Q. Lu, Y. Li, M. Zhao, J. Wang, Y. Li, J. Zhang, X. Zheng, X. Han, N. Zhao, J. Li, Y. Liu, Y. Deng and W. Hu, *J. Am. Chem. Soc.*, 2023, **145**, 1924–1935.

34 Q. Mao, X. Mu, K. Deng, H. Yu, Z. Wang, Y. Xu, X. Li, L. Wang and H. Wang, *Adv. Funct. Mater.*, 2023, **33**, 2304963.

35 H. Li, Y. Han, H. Zhao, W. Qi, D. Zhang, Y. Yu, W. Cai, S. Li, J. Lai, B. Huang and L. Wang, *Nat. Commun.*, 2020, **11**, 5437.

36 D. Zhang, Y. Shi, X. Chen, J. Lai, B. Huang and L. Wang, *Chin. J. Catal.*, 2023, **45**, 174–183.

37 D. Zhang, Y. Shi, H. Zhao, W. Qi, X. Chen, T. Zhan, S. Li, B. Yang, M. Sun, J. Lai, B. Huang and L. Wang, *J. Mater. Chem. A*, 2021, **9**, 889–893.

38 X. Fu, J. Zhang, S. Zhan, F. Xia, C. Wang, D. Ma, Q. Yue, J. Wu and Y. Kang, *ACS Catal.*, 2022, **12**, 11955–11959.

39 R. K. Nutor, Q. Cao, X. Wang, D. Zhang, Y. Fang, Y. Zhang and J.-Z. Jiang, *Adv. Eng. Mater.*, 2020, **22**, 2000466.

40 Y. Zhang, Y. J. Zhou, J. P. Lin, G. L. Chen and P. K. Liaw, *Adv. Eng. Mater.*, 2008, **10**, 534–538.

41 X. Yang and Y. Zhang, *Mater. Chem. Phys.*, 2012, **132**, 233–238.

42 S. Guo, C. Ng, J. Lu and C. T. Liu, *J. Appl. Phys.*, 2011, **109**, 103505.

43 S. Guo and C. T. Liu, *Prog. Nat. Sci.:Mater. Int.*, 2011, **21**, 433–446.

44 S. Fang, X. Xiao, L. Xia, W. Li and Y. Dong, *J. Non-Cryst. Solids*, 2003, **321**, 120–125.

45 Y. F. Ye, Q. Wang, J. Lu, C. T. Liu and Y. Yang, *Scr. Mater.*, 2015, **104**, 53–55.

46 G. A. Mansoori, N. F. Carnahan, K. E. Starling and T. W. Leland, Jr., *J. Chem. Phys.*, 1971, **54**, 1523–1525.

47 A. K. Singh, N. Kumar, A. Dwivedi and A. Subramaniam, *Intermetallics*, 2014, **53**, 112–119.

48 Z. Wang, Y. Huang, Y. Yang, J. Wang and C. T. Liu, *Scr. Mater.*, 2015, **94**, 28–31.

49 Y. Wu, P. K. Liaw, R. Li, W. Zhang, G. Geng, X. Yan, G. Liu and Y. Zhang, *Int. J. Miner., Metall. Mater.*, 2024, **31**, 1350–1363.

50 S. Guo, *Mater. Sci. Technol.*, 2015, **31**, 1223–1230.

51 I. Toda-Caraballo and P. E. J. Rivera-Díaz-del-Castillo, *Intermetallics*, 2016, **71**, 76–87.

52 M. G. Poletti and L. Battezzati, *Acta Mater.*, 2014, **75**, 297–306.

53 Z. Pei, J. Yin, J. A. Hawk, D. E. Alman and M. C. Gao, *npj Comput. Mater.*, 2020, **6**, 50.

54 Y. Zhang, C. Wen, C. Wang, S. Antonov, D. Xue, Y. Bai and Y. Su, *Acta Mater.*, 2020, **185**, 528–539.

55 Y. Zeng, M. Man, K. Bai and Y.-W. Zhang, *Mater. Des.*, 2021, **202**, 109532.

56 M. C. Troparevsky, J. R. Morris, P. R. C. Kent, A. R. Lupini and G. M. Stocks, *Phys. Rev. X*, 2015, **5**, 011041.

57 W. Chen, A. Hilhorst, G. Bokas, S. Gorsse, P. J. Jacques and G. Hautier, *Nat. Commun.*, 2023, **14**, 2856.

58 X. Chang, M. Zeng, K. Liu and L. Fu, *Adv. Mater.*, 2020, **32**, 1907226.

59 F. Zhang, Y. Wu, H. Lou, Z. Zeng, V. B. Prakapenka, E. Greenberg, Y. Ren, J. Yan, J. S. Okasinski, X. Liu, Y. Liu, Q. Zeng and Z. Lu, *Nat. Commun.*, 2017, **8**, 15687.

60 K. Xiong, L. Huang, X. Wang, L. Yu and W. Feng, *Metals*, 2022, **12**, 1254.

61 H. Luo, Z. Li, A. M. Mingers and D. Raabe, *Corros. Sci.*, 2018, **134**, 131–139.

62 Q. Zhao, Z. Pan, X. Wang, H. Luo, Y. Liu and X. Li, *Corros. Sci.*, 2022, **208**, 110666.

63 Y. Shi, B. Yang, X. Xie, J. Brechtl, K. A. Dahmen and P. K. Liaw, *Corros. Sci.*, 2017, **119**, 33–45.

64 Y. Fu, J. Li, H. Luo, C. Du and X. Li, *J. Mater. Sci. Technol.*, 2021, **80**, 217–233.

65 C. P. Lee, C. C. Chang, Y. Y. Chen, J. W. Yeh and H. C. Shih, *Corros. Sci.*, 2008, **50**, 2053–2060.

66 B. Ren, Z. X. Liu, D. M. Li, L. Shi, B. Cai and M. X. Wang, *Mater. Corros.*, 2012, **63**, 828–834.

67 Y. Maruta, K. Kusada, D. Wu, T. Yamamoto, T. Toriyama, S. Matsumura, O. Seo, S. Yasuno, S. Kawaguchi, O. Sakata, Y. Kubota and H. Kitagawa, *Chem. Commun.*, 2022, **58**, 6421–6424.

68 Y. Wang, M. Jiao, Y. Wu, X. Liu, H. Wang, S. Jiang, X. Zhang and Z. Lu, *J. Mater. Sci. Technol.*, 2024, **180**, 23–31.

69 K. Liu, H. Yang, Y. Jiang, Z. Liu, S. Zhang, Z. Zhang, Z. Qiao, Y. Lu, T. Cheng, O. Terasaki, Q. Zhang and C. Gao, *Nat. Commun.*, 2023, **14**, 2424.

70 W. Chen, C. Hu, J. Li, S. He, H. Liu and Z. Hua, *Langmuir*, 2025, **41**, 14345–14359.

71 G. Zhang, K. Ming, J. Kang, Q. Huang, Z. Zhang, X. Zheng and X. Bi, *Electrochim. Acta*, 2018, **279**, 19–23.

72 C.-Y. Wu, C.-Y. Wu, Y.-C. Hsiao and T.-H. Yang, *J. Electron. Mater.*, 2025, **54**(9), 7401–7422.

73 Z. Huang, T. Cheng, A. H. Shah, G. Zhong, C. Wan, P. Wang, M. Ding, J. Huang, Z. Wan, S. Wang, J. Cai, B. Peng, H. Liu, Y. Huang, W. A. Goddard and X. Duan, *Nat. Catal.*, 2024, **7**, 678–688.

74 Z. Chen, J. Wen, C. Wang and X. Kang, *Small*, 2022, **18**, 2204255.

75 Y. Kang, O. Cretu, J. Kikkawa, K. Kimoto, H. Nara, A. S. Nugraha, H. Kawamoto, M. Eguchi, T. Liao, Z. Sun, T. Asahi and Y. Yamauchi, *Nat. Commun.*, 2023, **14**, 4182.

76 Y.-C. Hsiao, C.-Y. Wu, C.-H. Lee, W.-Y. Huang, H. V. Thang, C.-C. Chi, W.-J. Zeng, J.-Q. Gao, C.-Y. Lin, J.-T. Lin, A. M. Gardner, H. Jang, R.-H. Juang, Y.-H. Liu, I. M. A. Mekhemer, M.-Y. Lu, Y.-R. Lu, H.-H. Chou, C.-H. Kuo, S. Zhou, L.-C. Hsu, H.-Y. T. Chen, A. J. Cowan, S.-F. Hung, J.-W. Yeh and T.-H. Yang, *Adv. Mater.*, 2025, **37**, 2411464.

77 Y. Yao, Z. Huang, P. Xie, S. D. Lacey, R. J. Jacob, H. Xie, F. Chen, A. Nie, T. Pu, M. Rehwoldt, D. Yu, M. R. Zachariah, C. Wang, R. Shahbazian-Yassar, J. Li and L. Hu, *Science*, 2018, **359**, 1489–1494.

78 M. Liu, Z. Zhang, F. Okejiri, S. Yang, S. Zhou and S. Dai, *Adv. Mater. Interfaces*, 2019, **6**, 1900015.

79 S. Gao, S. Hao, Z. Huang, Y. Yuan, S. Han, L. Lei, X. Zhang, R. Shahbazian-Yassar and J. Lu, *Nat. Commun.*, 2020, **11**, 2016.

80 X. Wang, Q. Peng, X. Zhang, X. Lv, X. Wang and Y. Fu, *J. Colloid Interface Sci.*, 2022, **607**, 1580–1588.

81 L. Jing, Y. Zou, R. Goei, L. Wang, J. A. Ong, A. Kurkin, Y. Li, K. W. Tan and A. I. Y. Tok, *Langmuir*, 2023, **39**, 3142–3150.

82 Y. Liao, R. Zhu, W. Zhang, H. Zhu, Y. Sun, J. Chen, Z. Dong and R. Lv, *Nano Res.*, 2024, **17**, 3379–3389.

83 Y. Wang, Y. Zhang, P. Xing, X. Li, Q. Du, X. Fan, Z. Cai, R. Yin, Y. Yao and W. Gan, *Adv. Mater.*, 2024, **36**, 2402391.

84 J.-H. Cha, S.-H. Cho, D.-H. Kim, D. Jeon, S. Park, J.-W. Jung, I.-D. Kim and S.-Y. Choi, *Adv. Mater.*, 2023, **35**, 2305222.

85 Z.-X. Cai, H. Goou, Y. Ito, T. Tokunaga, M. Miyauchi, H. Abe and T. Fujita, *Chem. Sci.*, 2021, **12**, 11306–11315.

86 Z. Jin, J. Lyu, Y.-L. Zhao, H. Li, X. Lin, G. Xie, X. Liu, J.-J. Kai and H.-J. Qiu, *ACS Mater. Lett.*, 2020, **2**, 1698–1706.

87 Y. Wang, B. Yu, M. He, Z. Zhai, K. Yin, F. Kong and Z. Zhang, *Nano Res.*, 2022, **15**, 4820–4826.

88 J. Kwon, S. Sun, S. Choi, K. Lee, S. Jo, K. Park, Y. K. Kim, H. B. Park, H. Y. Park, J. H. Jang, H. Han, U. Paik and T. Song, *Adv. Mater.*, 2023, **35**, 2300091.

89 T. Zhang, J. Li, B. Zhang, G. Wang, K. Jiang, Z. Zheng and J. Shen, *J. Alloys Compd.*, 2023, **969**, 172439.

90 H. Zhu, S. Sun, J. Hao, Z. Zhuang, S. Zhang, T. Wang, Q. Kang, S. Lu, X. Wang, F. Lai, T. Liu, G. Gao, M. Du and D. Wang, *Energy Environ. Sci.*, 2023, **16**, 619–628.

91 D. Kim, S. Surendran, Y. Jeong, Y. Lim, S. Im, S. Park, J. Y. Kim, S. Kim, T.-H. Kim, B. Koo, K. Jin and U. Sim, *Adv. Mater. Technol.*, 2023, **8**, 2200882.

92 M. W. Glasscott, A. D. Pendergast, S. Goines, A. R. Bishop, A. T. Hoang, C. Renault and J. E. Dick, *Nat. Commun.*, 2019, **10**, 2650.

93 Y. Wang, W. Luo, S. Gong, L. Luo, Y. Li, Y. Zhao and Z. Li, *Adv. Mater.*, 2023, **35**, 2302499.

94 Y. Lu, K. Huang, X. Cao, L. Zhang, T. Wang, D. Peng, B. Zhang, Z. Liu, J. Wu, Y. Zhang, C. Chen and Y. Huang, *Adv. Funct. Mater.*, 2022, **32**, 2110645.

95 X. Zhou, L. Zou, H. Zhu, M. Yan, J. Wang, S. Lan, S. Chen, H. Hahn and T. Feng, *Small*, 2023, 2310327.

96 B. Wang, C. Wang, X. Yu, Y. Cao, L. Gao, C. Wu, Y. Yao, Z. Lin and Z. Zou, *Nat. Synth.*, 2022, **1**, 138–146.

97 Q. Gao, Z. Wang, W. Gao and H. Yin, *Chem. Eng. J.*, 2024, **489**, 151370.

98 S. Wang, B. Xu, W. Huo, H. Feng, X. Zhou, F. Fang, Z. Xie, J. K. Shang and J. Jiang, *Appl. Catal., B*, 2022, **313**, 121472.

99 P. Ma, M. Zhao, L. Zhang, H. Wang, J. Gu, Y. Sun, W. Ji and Z. Fu, *J. Materiomics*, 2020, **6**, 736–742.

100 G. Lee, N.-A. Nguyen, V.-T. Nguyen, L. L. Larina, E. Chuluunbat, E. Park, J. Kim, H.-S. Choi and M. Keidar, *J. Solid State Chem.*, 2022, **314**, 123388.

101 S. Ding, Y. Sun, F. Lou, L. Yu, B. Xia, J. Duan, Y. Zhang and S. Chen, *J. Power Sources*, 2022, **520**, 230873.

102 D. Lai, Q. Kang, F. Gao and Q. Lu, *J. Mater. Chem. A*, 2021, **9**, 17913–17922.

103 H. Minamihara, K. Kusada, D. Wu, T. Yamamoto, T. Toriyama, S. Matsumura, L. S. R. Kumara, K. Ohara, O. Sakata, S. Kawaguchi, Y. Kubota and H. Kitagawa, *J. Am. Chem. Soc.*, 2022, **144**, 11525–11529.

104 M. Wei, Y. Sun, J. Zhang, F. Ai, S. Xi and J. Wang, *Energy Environ. Sci.*, 2023, **16**, 4009–4019.

105 R. Nandan, M. Y. Rekha, H. R. Devi, C. Srivastava and K. K. Nanda, *Chem. Commun.*, 2021, **57**, 611–614.

106 H. Wu, Q. Lu, Y. Li, J. Wang, Y. Li, R. Jiang, J. Zhang, X. Zheng, X. Han, N. Zhao, J. Li, Y. Deng and W. Hu, *Nano Lett.*, 2022, **22**, 6492–6500.

107 X. Lin, Y. Hu, K. Hu, X. Lin, G. Xie, X. Liu, K. M. Reddy and H.-J. Qiu, *ACS Mater. Lett.*, 2022, **4**, 978–986.

108 H.-J. Qiu, G. Fang, J. Gao, Y. Wen, J. Lv, H. Li, G. Xie, X. Liu and S. Sun, *ACS Mater. Lett.*, 2019, **1**, 526–533.

109 H. Zhu, Z. Zhu, J. Hao, S. Sun, S. Lu, C. Wang, P. Ma, W. Dong and M. Du, *Chem. Eng. J.*, 2022, **431**, 133251.

110 Y. Sun, W. Wu, L. Yu, S. Xu, Y. Zhang, L. Yu, B. Xia, S. Ding, M. Li, L. Jiang, J. Duan, J. Zhu and S. Chen, *Carbon Energy*, 2023, **5**, e263.

111 K. Huang, B. Zhang, J. Wu, T. Zhang, D. Peng, X. Cao, Z. Zhang, Z. Li and Y. Huang, *J. Mater. Chem. A*, 2020, **8**, 11938–11947.

112 L.-H. Liu, N. Li, M. Han, J.-R. Han and H.-Y. Liang, *Rare Met.*, 2022, **41**, 125–131.

113 S. Li, X. Tang, H. Jia, H. Li, G. Xie, X. Liu, X. Lin and H.-J. Qiu, *J. Catal.*, 2020, **383**, 164–171.

114 Y. Yao, Z. Huang, T. Li, H. Wang, Y. Liu, H. S. Stein, Y. Mao, J. Gao, M. Jiao, Q. Dong, J. Dai, P. Xie, H. Xie, S. D. Lacey, I. Takeuchi, J. M. Gregoire, R. Jiang, C. Wang, A. D. Taylor, R. Shahbazian-Yassar and L. Hu, *Proc. Natl. Acad. Sci. U. S. A.*, 2020, **117**, 6316–6322.

115 T. Li, Y. Yao, B. H. Ko, Z. Huang, Q. Dong, J. Gao, W. Chen, J. Li, S. Li, X. Wang, R. Shahbazian-Yassar, F. Jiao and L. Hu, *Adv. Funct. Mater.*, 2021, **31**, 2010561.

116 Y. Chen, X. Zhan, S. L. A. Bueno, I. H. Shafei, H. M. Ashberry, K. Chatterjee, L. Xu, Y. Tang and S. E. Skrabalak, *Nanoscale Horiz.*, 2021, **6**, 231–237.

117 H. Jiang, X. Liu, M.-N. Zhu, J. Xu, L. An, P.-F. Sui, J.-L. Luo and G. J. Cheng, *Sci. Adv.*, 2022, **8**, eabm6541.

118 G. Zhu, Y. Jiang, H. Yang, H. Wang, Y. Fang, L. Wang, M. Xie, P. Qiu and W. Luo, *Adv. Mater.*, 2022, **34**, 2110128.

119 W. Chen, S. Luo, M. Sun, X. Wu, Y. Zhou, Y. Liao, M. Tang, X. Fan, B. Huang and Z. Quan, *Adv. Mater.*, 2022, **34**, 2206276.

120 T. Mushiana, M. Khan, M. I. Abdullah, N. Zhang and M. Ma, *Nano Res.*, 2022, **15**, 5014–5023.

121 M. Li, C. Huang, H. Yang, Y. Wang, X. Song, T. Cheng, J. Jiang, Y. Lu, M. Liu, Q. Yuan, Z. Ye, Z. Hu and H. Huang, *ACS Nano*, 2023, **17**, 13659–13671.

122 S. Qi, Z. Lei, Q. Huo, J. Zhao, T. Huang, N. Meng, J. Liao, J. Yi, C. Shang, X. Zhang, H. Yang, Q. Hu and C. He, *Adv. Mater.*, 2024, **36**, 2403958.

123 N. Kar, M. McCoy, J. Wolfe, S. L. A. Bueno, I. H. Shafei and S. E. Skrabalak, *Nat. Synth.*, 2024, **3**, 175–184.

124 J. Sun, A. Leff, Y. Li and T. J. Woehl, *Nanoscale*, 2023, **15**, 10447–10457.

125 G. R. Dey, C. R. McCormick, S. S. Soliman, A. J. Darling and R. E. Schaak, *ACS Nano*, 2023, **17**, 5943–5955.